arXiv:1104.4122v1 [astro-ph.CO] 20 Apr 2011

# THE SUPER-LINEAR SLOPE OF THE SPATIALLY-RESOLVED STAR FORMATION LAW IN NGC 3521 AND NGC 5194 (M51A)

Guilin Liu[1], Jin Koda[2], Daniela Calzetti[1], Masayuki Fukuhara[3], and Rieko Momose[3,4]

*Accepted for publication in ApJ*

## ABSTRACT

We have conducted interferometric observations with the Combined Array for Research in Millimeter Astronomy (CARMA) and an on-the-fly mapping with the 45-m telescope at Nobeyama Radio Observatory (NRO45) in the CO ($J$=1–0) emission line of the nearby spiral galaxy NGC 3521. Using the new combined CARMA + NRO45 data of NGC 3521, together with similar data for NGC 5194 (M51a) and archival SINGS H$\alpha$, 24 $\mu$m, THINGS H I and GALEX FUV data for these two galaxies, we investigate the empirical scaling law that connects the surface density of star formation rate (SFR) and cold gas (known as the Schmidt-Kennicutt law or S-K law) on a spatially-resolved basis, and find a super-linear slope for the S-K law when carefully subtracting the background emissions in the SFR image. We argue that plausibly deriving SFR maps of nearby galaxies requires the diffuse stellar and dust background emission to be subtracted carefully (especially in the mid-infrared and to a lesser extent in the FUV). Applying this approach, we perform a pixel-by-pixel analysis on both galaxies and quantitatively show that the controversial results whether the molecular S-K law (expressed as $\Sigma_{\mathrm{SFR}} \propto \Sigma_{\mathrm{H_2}}^{\gamma_{\mathrm{H_2}}}$) is super-linear or basically linear is a result of removing or preserving the local background. In both galaxies, the power index of the molecular S-K law is super-linear ($\gamma_{\mathrm{H_2}} \gtrsim 1.5$) at the highest available resolution ($\sim$230 pc), and decreases monotonically for decreasing resolution. We also find in both galaxies that the scatter of the molecular S-K law ($\sigma_{\mathrm{H_2}}$) monotonically increases as the resolution becomes higher, indicating a trend for which the S-K law breaks down below some scale. Both $\gamma_{\mathrm{H_2}}$ and $\sigma_{\mathrm{H_2}}$ are systematically larger in M51a than in NGC 3521, but when plotted against the *de-projected* scale ($\delta_{\mathrm{dp}}$), both quantities become highly consistent for the two galaxies, tentatively suggesting that the sub-kpc molecular S-K law in spiral galaxies depends only on the scale being considered, without varying amongst spiral galaxies. A logarithmic function $\gamma_{\mathrm{H_2}} = -1.1 \log[\delta_{\mathrm{dp}}/\mathrm{kpc}] + 1.4$ and a linear relation $\sigma_{\mathrm{H_2}} = -0.2 [\delta_{\mathrm{dp}}/\mathrm{kpc}] + 0.7$ are obtained through fitting to the M51a data, which describes both galaxies impressively well on sub-kpc scales. A larger sample of galaxies with better sensitivity, resolution and broader field of view are required to test the general applicability of these relations.

*Subject headings:* galaxies: individual (NGC 3521, NGC 5194, M51a); galaxies: ISM; galaxies: spiral; ISM: molecules; radio lines: galaxies, Stars: Formation

## 1. INTRODUCTION

Much of the information we obtain on galaxies and their evolution is the consequence of the formation of stars, the process that depletes galaxies of their gas, dynamically energizes the stellar disks and enriches the interstellar medium with heavy elements through generations of evolving stars. Despite its fundamental importance on nearly all scales of astronomy, star formation is an exceedingly complex process to explore in the *ab initio* manner as a result of the many entangling aspects including the dynamical, geometrical, magnetic and chemical properties of ISM, as well as the feedback that the young stellar objects exert on their surrounding environment by radiation, stellar wind and explosion of supernovae.

In spite of this difficulty, the well-established empirical scaling laws of star formation that connect the large-

scale star formation rate (SFR) to interstellar medium (ISM) properties already play a crucial role in establishing plausible scenarios for galaxy evolution, and serve as essential prescription in modeling and simulating galaxy formation and evolution. Among them, the most widely adopted power-law relationship known as Schmidt law (Schmidt 1959) links the volume or surface density of SFR to that of the gas (Kennicutt 1989). From an observational point of view, a variety of SFR indicators are currently used, along with gas density information derived from emission lines of molecules (e.g. CO, HCN), to trace the relation between the birthrate of stars and their environment. By averaging over the whole disk of individual galaxies and taking the total (atomic + molecular) cold gas into account, a single power-law scaling between the surface density of star formation and gas (the Schmidt-Kennicutt law, abbreviated as the S-K law; Kennicutt 1998) extending over five orders of magnitude in the gas density has been well established, taking the form $\Sigma_{\mathrm{SFR}} \propto \Sigma_{\mathrm{gas}}^{1.4\pm0.15}$ where $\Sigma_{\mathrm{SFR}}$ (in M$_\odot$ yr$^{-1}$ kpc$^{-2}$) and $\Sigma_{\mathrm{gas}}$ (in M$_\odot$ pc$^{-2}$) denote the disk-averaged SFR and gas surface density, respectively.

Both parameters in this equation are, however, *global* quantities averaging over local values that may vary

[1] Astronomy Department, University of Massachusetts, Amherst, MA 01003-9305, USA
[2] Department of Physics and Astronomy, SUNY Stony Brook, Stony Brook, NY 11794-3800, USA
[3] Department of Astronomy, University of Tokyo, Hongo, Bunkyo-ku, Tokyo 113-0033, Japan
[4] National Astronomical Observatory of Japan, Mitaka, Tokyo 181-8588, Japan

by several orders of magnitude. Further understanding of star formation on a more physical basis requires scrutinizing galaxies at the sub-galactic scale. Limited by development of the relevant instrumentation, spatially-resolved investigations of the gas content of individual star-forming sites have become a front-line topic only in recent years (e.g., Wong & Blitz 2002; Boissier et al. 2003; Heyer et al. 2004; Kennicutt et al. 2007; Bigiel et al. 2008; Blanc et al. 2009). Spatially-resolved studies promise to yield insights into the physical processes driving the scaling laws, much more directly than the disk-averaged results. Measuring the star formation and gas at sub-kpc scales requires high resolution and sensitivity, which are currently available only for small or limited samples both for atomic hydrogen (e.g., through THINGS; Walter et al. 2008) or molecular hydrogen (via CO, e.g., HERACLES; Leroy et al. 2009). Observational studies on the slope of the local S-K law in a handful of nearby galaxies result in power-law indices of 1–3 (reviewed by, e.g., Elmegreen 2002; Bigiel et al. 2008), where the cold gas mass in both atomic and molecular phases are taken into account. However, in recent times, it has become clearer that star formation activity, at least on local scales, is much less correlated with H I than with CO (Kennicutt et al. 2007; Bigiel et al. 2008, hereafter K07 and B08, respectively), which suggests that further investigations on the power law index of the S-K law should concentrate on the scaling relationship between SFR and molecular gas.

The availability of high resolution and sensitivity maps for CO as the most commonly used molecular hydrogen tracer thus provide the main actual limitation to sub-kpc studies of star formation scaling laws. In general, interferometric CO maps have higher resolution (typically a few arcseconds) and are powerful in resolving fine structures, but their limited field of view (FoV) and the shortcoming of missing the zero spacing flux often downgrade their scientific value; on the other hand, despite that single-dish observations are time-saving (especially if On-The-Fly mapping techniques are introduced) and cover much wider FoVs, their larger beams often smear out the details of star forming sites. In recent years, along with use of mosaicing that improves the FoV of interferometry, the technique of compensating the absent short baselines components with single-dish data (at the price of losing some resolution) has been developed. With this technique mature, single-dish-compensated interferometric data of CO transition line maps become the best available molecular gas tracer for investigations of star formation scaling laws. In this direction, a new CARMA (the Combined Array for Research in Millimeter-wave Astronomy) & NRO45 (Nobeyama Radio Observatory 45m telescope) CO survey of nearby galaxies is underway (Koda et al. 2009b) with the goal of better understanding the evolution of the ISM, galactic dynamics, and the star formation laws. Included in the sample of this CO survey, one of our program galaxies, NGC 3521, is mapped by CARMA with a $3.65'' \times 3.14''$ synthesized beam and by NRO45 using a $18.4''$ beam, leading to a final resolution of $5.43'' \times 4.68''$ when the two sets of data are combined in $uv$-space with the new technique established by Koda et al. (2009a). This CARMA + NRO45 survey not only isolates typical GMCs with its $\sim$220 pc resolution at a distance of $\sim$8 Mpc (a typical GMC separation is $\sim$200 pc in the Milky Way, Koda et al. 2006), but also detects the interarm extended emission at a high sensitivity ($1\sigma \sim 3$ M$_\odot$ pc$^{-2}$).

The other crucial parameter in the resolved S-K law study is the SFR. Over the past twenty to thirty years, extensive efforts have been made to plausibly derive SFRs (see Calzetti et al. (2010) for a review of the last decade and Kennicutt (1998) for earlier times). Conventional optical SFR tracers like H$\alpha$ often severely suffer from dust extinction ($A_V \sim 2.2$ mag in typical extragalactic H II regions, Calzetti et al. 2007), which changes drastically from location to location and can be completely obscured in dense star forming regions where $A_V$ can reach $\sim$6 mag (Scoville et al. 2001, for the case of M51a). Recent space-borne facilities have opened infrared (IR) and ultraviolet (UV) windows for star formation study. The Spitzer Infrared Nearby Galaxies Survey (SINGS, Kennicutt et al. 2003) and the GALEX Nearby Galaxies Survey (NGS, Bianchi et al. 2003a,b) enables us to image the details of dust obscured and unobscured star formation sites in parallel, so that both the dust reprocessed and directly emerging radiation from young stellar associations are measured. K07 and Calzetti et al. (2007) have justified the feasibility of correcting the number of ionizing photons (as traced by the H$\alpha$ recombination line) for the effects of dust extinction by adding a weighted component from the Spitzer MIPS 24 $\mu$m luminosity in individual star forming regions. This H$\alpha$+24 $\mu$m SFR motivated Leroy et al. (2008) and B08 to propose another composite SFR tracer that corrects dust attenuation of far-UV (FUV) surface brightness using the same mid-IR component (but with different weights).

The extinction-corrected H$\alpha$ line emission has long been proved a reliable estimator of the rate of formation of young, massive stars, since stellar synthesis models show that for co-eval stellar populations with standard Initial Mass Functions that rate remains fairly constant for the first few million years ($\sim$5 Myr), and then abruptly fades away as massive stars become supernovae (Schaerer & de Koter 1997).

In marked contrast, a stellar population can emit in the continuum UV (longward of 1300 Å) for up to one order of magnitude longer timescale. The Local Volume Legacy (LVL) Survey team has found many dwarf galaxies that show little or no sign of dust and sporadic highly concentrated H$\alpha$ emission, yet show strong and extended UV emission and have red UV colors, consistent with stellar populations at the age of a few 100 Myrs (Dale et al. 2009). This complicates the comparison between H$\alpha$–based and UV-based SFR indicators. An in-depth discussion on the consistency and discrepancy of deriving SFR via H$\alpha$ and UV is presented in Lee et al. (2009).

The issue of a molecular-only S-K law is only now starting to be tackled. Several earlier attempts were made by utilizing azimuthally averaged data. Employing this strategy, Wong & Blitz (2002) studied seven CO-bright spiral galaxies and concluded that SFR is in direct proportion to molecular cloud density; Boissier et al. (2003) compiled the data for 16 galaxies and found the slope $\sim$0.6–1.3 (though most data points seemingly favor a super-linear slope; see Figure 10 therein); Heyer et al. (2004) examined the low-luminosity, molecule-poor M33

galaxy by combining 60 and 100 $\mu$m IR images with CO ($J$=1–0) single-dish line map, and suggested a power index of 1.36±0.08. More recently, SFR and molecular gas surface density have been compared on individual sub-kpc regions. K07 performed an analysis of star formation complexes in M51a (NGC 5194) and obtained a slope of 1.37±0.03 for the molecular S-K law at $\sim$500 pc resolution. On the other hand, B08 performed a pixel-by-pixel analysis (750 pc scale) for seven spiral galaxies and found a power index 1.0±0.2 or a linear molecular S-K law. Thus it can be seen that the results from different groups as yet fall into two categories: linear or super-linear scaling relation, which is still now under debate. Wong & Blitz (2002) would have obtained results similar to Heyer et al. (2004) if radially dependent extinction corrections were applied to their H$\alpha$ data. B08 qualitatively suggests that the inconsistency between their results and K07 is likely an effect of removal of the local background emission in the K07 photometry of the SFR tracers. Clearly, background subtractions in the SFR maps is a crucial component for the investigation of star formation laws.

In parallel to these observational efforts, various star formation models have been constructed, generally assuming one mechanism that dominates the formation process. Among these models, a postulated constant star formation efficiency independent of the environment will lead to a linear relation (Leroy et al. 2008), in which case the mere presence of the gas is sufficient for star formation; a slope of 1.5 will be found if star formation is driven by large scale gravitational instabilities, and thus occurs in a dynamical (free-fall) timescale of molecular gas (Elmegreen 2002); cloud-cloud collisions will drive the slope to be as steep as $\sim$2 (Tasker & Tan 2009); other considered mechanisms include global resonances (Wyse & Silk 1989), galactic shear (Hunter et al. 1998), dust shielding (Gnedin et al. 2009), turbulence (Krumholz et al. 2009) and others (for reviews, see Elmegreen 2002; McKee & Ostriker 2007; Tan 2010).

In this paper, we present a study of the sub-kpc S-K law in two nearby galaxies, NGC 3521 and M51a (NGC 5194). K07 and B08, despite sharing data sets for M51a, obtain different power law indices (super-linear vs. linear) of the molecular-only and total-hydrogen S-K laws. By employing a new method of local background subtraction, we show quantitatively that including or removing the local background in the maps tracing the SFR has a profound effect on the final results in M51a, as discussed in B08. By analyzing our high quality data, we infer that the linear correlation found by B08 for the molecular S-K law is a consequence of inclusion of stellar local background unrelated to current star formation. Throughout this paper, we base our analysis on the H$\alpha$+24 $\mu$m approach of calibrating SFRs, albeit the FUV+24$\mu$m SFR is included for the purpose of comparison.

Among the extensive measurements of the distance to these two nearby galaxies, we adopt the values from the compilation by the LVL survey group: 8.03 Mpc for NGC 3521 (from the flow-field corrected recessional velocity, assuming $H_0$=75 km s$^{-1}$ Mpc$^{-1}$; Kennicutt et al. 2008), and 8.00 Mpc for M51a (by direct distance measurement of the M51 group, Karachentsev et al. 2004).

NGC 3521 and M51a possess similar properties in several aspects. First of all, the disk-average SFR surface density is $\sim$0.0026 M$_\odot$ yr$^{-1}$ kpc$^{-2}$ and $\sim$0.0057 M$_\odot$ yr$^{-1}$ kpc$^{-2}$ for these two spirals, respectively (Calzetti et al. 2010), characterizing both as quiescently star-forming systems. Moreover, both galaxies are shown to be metal-rich from spectroscopic measurements, with 12+log(O/H) values 9.01 for NGC 3521 and 9.18 for M51a (Moustakas et al. 2010). In addition, classified as SABbc in the Hubble sequence (RC3, de Vaucouleurs et al. 1991), NGC 3521, with an inclination of 72.7° (de Blok et al. 2008), is a flocculent-type spiral galaxy that has a tightly wound two-arm pattern (Thornley 1996), while its much less inclined peer M51a ($i = 42°$, Tamburro et al. 2008), a grand-design spiral of morphological type SAbc, shows a prominent two-arm configuration. The virtually identical size of their galactic disks is a consequence of having almost identical distances ($\sim$8 Mpc) and apparent size in the H$\alpha$ images that depicts unambiguously the spiral arms (284$''$ and 296$''$ in radius, respectively). These facts, when summed together, suggest that the two star–forming disks are very similar, with the major difference being their inclinations. This is an important ingredient for understanding the influence of spatial resolution on the resultant shape of star formation laws (see the result and discussion section).

The paper is organized as follows: section 2 describes the data and, especially for the CARMA/NRO45 data, provides some detail on the observations and data reduction; section 3 presents our new method of automated local background removal which enables our pixel-by-pixel analysis to reproduce both the results of K07 and B08 accurately, and discusses the necessity of local background removal; section 4 is devoted to applying our strategy to both spirals to test the behavior of the sub-kpc star formation laws; the results are discussed in section 5 and summarized in section 6.

## 2. DATA

In Figure 1 we show the H$\alpha$ (KPNO 2.1-m telescope), 24 $\mu$m (Spitzer SINGS survey), CO (our CARMA observation) and FUV (GALEX NGS survey) images for NGC 3521. More technical details of these data and the CARMA + NRO45 CO map of M51a are given in the following subsections. The H$\alpha$, 24 $\mu$m, BIMA SONG CO and FUV images of M51a, shared with K07 and B08, have been thouroughly described in those papers and details will only be provided when necessary. To compare our analysis with those in previous studies, we use the BIMA SONG data which were used in those studies, but our CARMA + NRO45 data are employed for further investigations.

### 2.1. *CARMA and NRO45 CO (J=1–0) Data*

The CO ($J$=1–0) interferometric observations of NGC 3521 were undertaken using the Combined Array for Research in Millimeter Astronomy (CARMA) from February to March in 2009. CARMA is the combination of the six 10 m antennas of the Owens Valley Radio Observatory (OVRO) millimeter interferometer and the nine 6 m antennas of the Berkeley-Illinois-Maryland Association (BIMA) interferometer. The entire optical disk

of NGC 3521 ($11.0' \times 5.1'$) was mosaiced in 19 pointings with Nyquist sampling of the 10 m antenna beam (FWHM of $1'$ for the 115 GHz CO $J$=1–0 line). The data were reduced and calibrated using the Multichannel Image Reconstruction, Image Analysis, and Display (MIRIAD) software package (Sault et al. 1995).

We also obtained total power and short-spacing data with the 25-Beam Array Receiver System (BEARS) on the Nobeyama Radio Observatory 45 m telescope (NRO45, FWHM = $15''$). Using the On-The-Fly observing mode (Sawada et al. 2008), the data were oversampled on a $5''$ lattice and then re-gridded with a spheroidal smoothing function, resulting in a final resolution of $18.4''$. Data reduction was performed using the NOSTAR data reduction package developed at the Nobeyama observatory. We constructed visibilities by deconvolving the NRO45 maps with the beam function (i.e., a convolution of the $15''$ Gaussian and spheroidal function), and Fourier transforming them to the $uv$-space. After that, we combined the CARMA and NRO45 data in Fourier space, inverted the $uv$ data using theoretical noise and natural weighting, and CLEANed the maps.

Throughout this paper, we adopt a CO-to-H$_2$ conversion factor of $X_{\mathrm{CO}}$=$2.8 \times 10^{20}$ cm$^{-2}$ (K km s$^{-1}$)$^{-1}$ (Bloemen et al. 1986) for NGC 3521 and M51a. The validity of this Galactic factor is justified by the supersolar abundance averaged over the galactic disks ($12 + \log(\mathrm{O/H}) = 9.01 \pm 0.02$ for NGC 3521, and $9.18 \pm 0.01$ for M51a, Moustakas et al. 2010). Additionally, the small metallicity gradients across the disk justifies the application of a single value (Bresolin et al. 2004).

For NGC 3521 at the distance of 8.03 Mpc, the angular resolution of the combined data ($5.4'' \times 4.7''$) corresponds to a physical scale of $\sim$220 pc, and the r.m.s. sensitivity (32 mJy beam$^{-1}$) in the 5.08 km s$^{-1}$ wide channels translates to a 3-$\sigma$ level of 2.4 M$_\odot$ pc$^{-2}$ at this resolution (assuming $i$=$72.7°$).

As for M51a, the detailed information of the CARMA + NRO45 observations and data reduction is described in Koda et al. (2009a) and Koda et al. (2011). At the final resolution of the combined map ($3.68'' \times 2.87''$, corresponding to $\sim$140 pc at a distance of 8.00 Mpc), the r.m.s. sensitivity (40 mJy beam$^{-1}$) in the 5.08 km s$^{-1}$ wide channels translates to a 3-$\sigma$ level of 18 M$_\odot$ pc$^{-2}$ (assuming $i$=$42°$). For comparison, the typical size of a GMC in the Galaxy is 50 to several hundred parsecs (Blitz 1993). We show a comparison between our combined CARMA + NRO45 and the BIMA SONG maps at a matched resolution, $5.8''$ (corresponding to 230 pc for M51a) in Figure 2. This highlights both the higher depth of our image and the fact that we recover substantial faint-level emission, which is absent from the BIMA SONG image.

## 2.2. *Hα Emission-Line Images*

NGC 3521 was imaged using the 2.1 m telescope at Kitt Peak National Observatory as part of the SINGS ancillary data program (Kennicutt et al. 2003). The Hα line is contaminated by the doublet [N II] $\lambda6548, 6584$. A ratio of $\lambda6548, 6584$/Hα=$0.55 \pm 0.03$ is adopted here to correct the data, following the integrated spectrophotometric survey of nearby star-forming galaxies accomplished by Moustakas et al. (2010). Our measurements

on the final emission-line-only Hα image has a PSF with a $1.4''$ FWHM. The sensitivity limit of the emission-line image is $2.5 \times 10^{-17}$ erg s$^{-1}$ cm$^{-2}$ arcsec$^{-2}$.

### 2.3. *Spitzer MIPS Images*

Spitzer MIPS 24 $\mu$m maps are available for NGC 3521, through the high level data products of the SINGS Legacy project (Spitzer Infrared Nearby Galaxy Survey, Kennicutt et al. 2003). The SINGS observation strategy, data reduction procedures, and map sensitivity limits are described in Kennicutt et al. (2003) and Dale et al. (2005). For MIPS 24 $\mu$m maps, the diffraction-limited angular resolution is $5.7''$ and the 1-$\sigma$ sensitivity limit $1.1 \times 10^{-6}$ Jy arcsec$^{-2}$.

### 2.4. *VLA H I Data*

The atomic hydrogen in NGC 3521 was mapped by the H I Nearby Galaxies Survey (THINGS, Walter et al. 2008) using the NRAO Very Large Array (VLA). The HI maps for our study are obtained through the THINGS public data release website[5]. The H I map, as a result of robust weighting, has a resolution of $8.19'' \times 6.41''$. In each of the 5.2 km s$^{-1}$ channels, the 1–$\sigma$ sensitivity is 0.47 mJy beam$^{-1}$, corresponding to a column density of $5.8 \times 10^{19}$cm$^{-2}$ or 0.5 M$_\odot$pc$^{-2}$ in the integrated map. The calibration error for the H I data are estimated to be $\sim$10%. Further technical details are given in Walter et al. (2008).

## 3. METHODOLOGY OF SPATIALLY-RESOLVED S-K LAW STUDIES

As mentioned in the Introduction, K07 and B08 find different results for the power law indices of the molecular S–K Law in M51a. B08 qualitatively point out that the difference arises because K07 subtract a local Hα and 24 $\mu$m background for each aperture, but different photometric approaches (K07: aperture photometry vs. B08: pixel-by-pixel) may also play a role. Meanwhile, such a test involves a highly tricky issue of local background removal. In this section, we present a new approach of local background determination. By using it, we quantitatively show that removing or preserving the local background is sufficient to account for the discrepancy between K07 and B08. From here onward, we will indicate the fits to the $\Sigma_{\mathrm{SFR}} - \Sigma_{\mathrm{H_2}}$ relation as

$$\frac{\Sigma_{\mathrm{SFR}}}{\mathrm{M_\odot \ yr^{-1} \ kpc^{-2}}} = A \left( \frac{\Sigma_{\mathrm{H_2}}}{\mathrm{M_\odot \ pc^{-2}}} \right)^{\gamma_{\mathrm{H_2}}} \qquad (1)$$

with $\gamma_{\mathrm{H_2}}$ indicating the power law exponent of the molecular gas surface density. The dispersion about the fitted relation will be indicated with $\sigma_{\mathrm{H_2}}$. The analogous relation for the total hydrogen gas will be indicated as

$$\frac{\Sigma_{\mathrm{SFR}}}{\mathrm{M_\odot \ yr^{-1} \ kpc^{-2}}} \propto \left( \frac{\Sigma_{\mathrm{H}}}{\mathrm{M_\odot \ pc^{-2}}} \right)^{\gamma_{\mathrm{H}}} \qquad (2)$$

where $\Sigma_{\mathrm{H}} = \Sigma_{\mathrm{HI}} + \Sigma_{\mathrm{H_2}}$. We also compare $\Sigma_{\mathrm{SFR(FUV+24\mu m)}}$ with $\Sigma_{\mathrm{SFR(H\alpha+24\mu m)}}$ through the relation

$$\Sigma_{\mathrm{SFR(FUV+24\mu m)}} \propto (\Sigma_{\mathrm{SFR(H\alpha+24\mu m)}})^{\gamma_{\mathrm{SFR}}}. \qquad (3)$$

---

[5] http://www.mpia-hd.mpg.de/THINGS/Overview.html

### 3.1. *Local Background Subtraction*

In the hydrogen line, FUV and mid-IR images used to trace SFR, besides the compact clumpy structures which trace of H II regions and young massive stars, there exists an underlying diffuse component of stellar/dust emission, which is conventionally referred to as "local background" with slight ambiguity. This convention continues in this paper, but we stress that the so-called "local background" here, apart from the local variation of sky or instrumental background, refers to the physical detection of the emission from stars or interstellar dust.

Pixel-by-pixel analysis introduces significant contamination from this local background especially in lower resolution images, in which case the low luminosity pixels can be more strongly affected than those at the bright end, effectively overestimating the SFRs at the faint end and thus flattening the slope of the scaling laws.

Conventional approaches to determine the local background levels in galaxies include performing statistics in an annular region, or fitting the galactic image with an assumed two-dimensional analytical function (e.g., polynomial, exponential, Sérsic profile or a combination of several galactic components). These methods work reasonably well in general but often fail in nearby galaxies because of the large dynamical range and crowding of clustered regions. Calzetti et al. (2005) and K07 defined 12 rectangular regions in the M51a images that they used as their "background" areas. Since it is not sensitive to local variations on smaller scales, this ad-hoc strategy produces reasonable results (see next subsection). However, a more automated approach is expected to enhance the reproduceability and robustness of the results. Blanc et al. (2009) identify and remove the diffuse ionized gas (DIG) from the Hα image of M51a statistically, based on Madsen et al. (2006) which demonstrate that the DIG in the Galaxy has a difference [S II]/Hα ratio (0.34) from that of Galactic H II regions (0.11). The Blanc et al. (2009) procedure has the advantage of being astrophysically motivated, but the DIG fraction recovered by these authors (11%) is smaller than that recovered by photometric measurements either when the whole galaxy (40–50%, e.g., Greenawalt et al. 1998; Thilker et al. 2000) or the central part of M51a is considered (we find the fraction to be 32% in the same central part covered by Blanc et al. 2009, using *HIIphot*).

In this work, we distinguish the compact component (presumably H II regions) from diffuse stellar/dust emission through morphological examination. This strategy is inevitably arbitrary to some extent, but its basic motivation has a strong physical underpinning. The properties of the diffuse Hα, 24 μm and UV emission have been extensively discussed by the existing literature, which is briefly reviewed in the discussion section. When such a strategy is being applied, the crowding of sources is the major obstacle to accurate background determination, but it can be circumvented by removing the compact clumps instead, which is done by adapting the algorithm of the IDL software *HIIphot* developed by Thilker et al. (2000) for our purposes in this work. The algorithm can be summarized as follows. On an Hα image of a galaxy, it identifies H II regions by smoothing the image with kernels of different sizes, and utilizes object recognition techniques to identify significant peaks ("seeds"). After

that, an iterative procedure is started allowing for area growth from these "seeds". The boundaries are built up at successively fainter isophotal levels that keep growing until either boundaries of other regions are encountered, or a pre-established lower limit to the gradient in surface brightness is reached implying its arrival at the background level. Two-dimension interpolations are then carried out by fitting the background pixels around each H II region to estimate the local background behind the source.

Originally designed for automated photometric characterization and statistical analysis of H II regions and their luminosity functions in Hα images, the algorithm of *HIIphot* can be easily adapted to 24 μm and FUV images. We tested our implementation of *HIIphot* on the HST Hα image of M51a, and produced an H II region luminosity function which is very similar to that of Scoville et al. (2001) (Liu et al. 2011). It should be noticed that our purpose of extracting star-forming regions against the local background is somewhat different from conventional Hα data analysis which aims at removing any contamination from diffuse components in H II regions. The lower limit gradient in surface brightness for the iterative growing procedure from the "seeds" is thus chosen to be sufficiently low (lower than what is typically chosen for H II region analysis) that we are confident to have reached an appropriate background level, but still sufficiently above zero to prevent growing deep into ambient areas.

Because of the much lower contribution from the diffuse emission in Hα than in mid-IR and FUV, the removal of the Hα local background is done conservatively, aiming at a background level to be reached only in the ambient area between the outer spiral arms. For the purpose of testing this approach, we also use a constant global background determined using several external H II regions in deriving S-K laws, and the resultant slopes differ minimally (< 0.1, typically ∼0.05).

The established source-free image is not smooth, but contains sharp edges at the boundaries of sources. We therefore smooth the image by calculating the median of the pixels enclosed in a moving box and replacing the central pixel with the median. Because of the robustness of the median in statistics, this smoothing technique leads to a relatively stable result and suffers much less from the steep local variations which will affect an image smoothed by kernel convolution. The size of the box is chosen as a compromise between minimization of the crater-like artifacts left by the removed H II regions and minimization of detail loss. The final resulting "diffuse emission" map is then ready for subtraction from the original image. The background-free images, along with the background images before and after the median smoothing, are shown in Figure 3 for the purpose of comparison. As can be seen from the figure, the background-free image mostly contains clustered sources, and the disk-like diffuse emission has been removed.

### 3.2. *Linear Relation without Local Background Subtraction*

B08 performed a pixel-by-pixel analysis on 7 spiral galaxies detected in CO ($J$=2–1) at a resolution of 750 pc including M51a. The employed SFR tracer in their study is a combination of far-UV and 24 μm luminosities

without local background subtraction and whose coefficients are adjusted to be consistent with the H$\alpha$+24 $\mu$m SFR tracer at 750 pc resolution, the applicability of which has been justified in K07 and Calzetti et al. (2007). No correlation between SFR and H I surface density is seen, a similar result to K07. In contrary to the super-linear relationship found by K07 (power law index $\gamma_{\mathrm{H_2}} = 1.37 \pm 0.03$), B08 find the surface density of SFRs to be proportional to that of molecular gas (power index $\gamma_{\mathrm{H_2}} = 1.0 \pm 0.2$). We notice that B08 carried out their analysis using CO ($J$=2–1) images from The HERA CO Line Extragalactic Survey (HERACLES; Leroy et al. 2009) except for M51a, for which they share the same data set as K07, including the CO ($J$=1–0) image from BIMA Survey of Nearby Galaxies (BIMA SONG; Helfer et al. 2003). This enables us to make a direct comparison of the two approaches of measurements adopted in these two studies to identify the reason for the discrepancy of the obtained power law indices.

The KPNO H$\alpha$, SINGS 24 $\mu$m, GALEX FUV, THINGS 21-cm H I and BIMA SONG CO ($J$=1–0) images of M51a have resolutions of 1.9″, 5.7″, 4.6″, 5.82″×5.56″ and 5.8″×5.1″, respectively. The 3-$\sigma$ sensitivity is 1.3 M$_\odot$ pc$^{-2}$ for the H I map (K07), and 13 M$_\odot$ pc$^{-2}$ for the CO map (Helfer et al. 2003). The 1-$\sigma$ detection limits of the 24 $\mu$m (1.1×10$^{-6}$ Jy arcsec$^{-2}$), H$\alpha$ (1.8×10$^{-17}$ erg s$^{-1}$ cm$^{-2}$ arcsec$^{-2}$) and FUV images (3.6×10$^{-19}$ erg s$^{-1}$ cm$^{-2}$Å$^{-1}$ arcsec$^{-2}$) (Calzetti et al. 2005) lead to a corresponding SFR$_{\mathrm{H\alpha+24\mu m}}$ of 1.0×10$^{-5}$ M$_\odot$ yr$^{-1}$ kpc$^{-2}$ and a SFR$_{\mathrm{FUV+24\mu m}}$ of 1.7 × 10$^{-5}$ M$_\odot$ yr$^{-1}$ kpc$^{-2}$ at 750 pc (19.3″) resolution. Here we have assumed an IMF given by Kroupa (2001) to derive the SFR surface density (in units of M$_\odot$ yr$^{-1}$ kpc$^{-2}$) following Calzetti et al. (2007) and Leroy et al. (2008):

$$\mathrm{SFR_{H\alpha+24\mu m}} = 5.3 \times 10^{-42} \, (L_{\mathrm{H\alpha}} + 0.031 \, L_{24\mu m}), \quad (4)$$

$$\mathrm{SFR_{FUV+24\mu m}} = 3.4 \times 10^{-44} \, (L_{\mathrm{FUV}} + 6.0 \, L_{24\mu m}), \quad (5)$$

where $L_{24\mu m}$ and $L_{\mathrm{FUV}}$, both defined as $\lambda L_\lambda$ and in units of erg s$^{-1}$, are referenced to the central wavelength of the Spitzer 24 $\mu$m ($\lambda$=23.68$\mu$m) and the GALEX FUV ($\lambda$=1528Å) filters, respectively.

We first convolve these M51a images with circular or elliptical 2-d gaussian kernels so that all the images are downgraded to a common physical resolution of 750 pc, the working scale of B08, for the purpose of comparison. Aligned to the astrometric frame of the 24 $\mu$m image which has the coarsest grid (1.5″), they are then regrided to a pixel scale of 750 pc to avoid sub-PSF sampling. The data are then converted to physical quantities, correlated pixel-by-pixel, and analyzed by linear fitting. In this study, the linear regressions are performed with the ordinary least square bisector method (same as K07 and B08), as recommended by Isobe et al. (1990).

The results for M51a are summarized in Figure 4 (the left of the panel pairs). At this resolution, we reproduce the results of B08 ($\gamma_{\mathrm{H_2,B08}}$=0.84) when FUV + 24 $\mu$m SFRs are correlated to molecular gas surface densities ($\gamma_{\mathrm{H_2}}$=0.83±0.04, Figure 4-b). we find a similar sublinear correlation ($\gamma_{\mathrm{H_2}}$=0.86±0.05) when using H$\alpha$+24 $\mu$m as a SFR indicator for the molecular-only S-K law (Figure 4-a), because of the tight, close-to-linear corre-

lation between SFR$_{\mathrm{FUV+24\mu m}}$ and SFR$_{\mathrm{H\alpha+24\mu m}}$ in the SFR $\gtrsim 10^{-3}$ M$_\odot$ yr$^{-1}$ kpc$^{-2}$ regime (a result of the calibration by Leroy et al. 2008, Figure 4-c). Nevertheless, the two SFR tracers correlate poorly with each other when SFR is lower than $10^{-3}$ M$_\odot$ yr$^{-1}$ kpc$^{-2}$, hinting at a discrepancy of deriving H$\alpha$ and UV at low surface brightnesses. All these linear fits have taken into account only those data points above their corresponding 3-$\sigma$ sensitivity limit which are shown in each panel as horizontal or vertical dotted lines.

Little or no correlation is found between SFR$_{\mathrm{FUV+24\mu m}}$ or SFR$_{\mathrm{H\alpha+24\mu m}}$ with the atomic gas surface density, and we observe a saturation at $\Sigma_{\mathrm{HI}} \sim 10$ M$_\odot$ pc$^{-2}$. Both effects had been already observed by both K07 and B08. An evident "kink" is seen at the transition from atomic- to molecular-dominated regimes when both components are combined to make a SFR – $\Sigma_{\mathrm{H}}$ comparison (Figure 4-e and 4-f). Compared to Figure 4-a or 4-b, the slope hardly changes in Figure 4-e ($\gamma_{\mathrm{H}}$=0.86±0.03, dashed line) where we restrict the fitting to pixels in which the total hydrogen surface density and SFR are above 3$\sigma$. However, when extended to the outer disk by assuming little or no existing molecules, the linear fit gives $\gamma_{\mathrm{H}}$=1.26±0.02, steeper than $\gamma_{\mathrm{H}}$=1.11 found by B08, a consequence of the fact that we do not mask the regions outside $D_{25}$. The results for M51a presented by B08 are therefore thouroughly reproduced by our independent pixel-by-pixel analysis.

We perform a similar comparison to B08's result for NGC 3521, although we use our CARMA + NRO45 CO ($J$=1-0) map, while those authors used their HERACLES CO ($J$=2-1) data. Since we adopt a smaller distance for this galaxy than B08 (8.03 Mpc vs. 10.7 Mpc for those authors), their assumed 750 pc pixels correspond in reality to 1 kpc pixels. We thus re-grid NGC 3521 to 1 kpc pixels and obtain a molecular-only power law index $\gamma_{\mathrm{H_2}} = 0.90 \pm 0.13$ when SFR is derived from H$\alpha$ and 24 $\mu$m data, or $\gamma_{\mathrm{H_2}} = 0.92 \pm 0.12$ when FUV is used instead (B08 find $\gamma_{\mathrm{H_2,B08}} = 0.95$). The SFRs derived in these two different ways coincides with each other, SFR$_{\mathrm{FUV+24\mu m}} \propto$ SFR$_{\mathrm{H\alpha+24\mu m}}^{1.02\pm0.02}$. The scaling relation for total hydrogen gas content gives $\gamma_{\mathrm{H}} = 2.06 \pm 0.31$ (without masking any part of the H I map), similar to B08's value of 2.12. We infer that the two different CO maps ($J$=1-0 and $J$=2-1) do not lead to discrepancies in the resulting S-K law, at least at the spatial scales investigated for this galaxy.

### 3.3. *Super-Linear Relation with Local Background Subtraction*

By employing both the extinction-corrected Pa$\alpha$ line image and the weighted sum of H$\alpha$ and 24 $\mu$m luminosities as an unbiased SFR tracer, K07 performed photometry using apertures with 13″ diameter (= 520 pc) on 257 positions in M51a where star formation is detected. The authors identified 12 rectangular areas and fit the local background for subtraction. This strategy was applied to both the hydrogen line image and the 24 $\mu$m map. As a result, a best-fit slope of $\gamma_{\mathrm{H}} = 1.56 \pm 0.04$ was found when the specific SFR is correlated to the total gas surface density on 520 pc scales; the slope decreases to 1.37±0.03 on 1850 pc scales. Additionally, virtually no correlation is seen between the local SFR surface density and the H I

surface density which saturates at log $[\Sigma_{HI}/M_\odot$ pc$^{-2}]\sim1$, while a strong correlation with a shallower best-fit slope of $\gamma_{H_2} = 1.37 \pm 0.03$ exists for the molecular S-K law on 520 pc.

The actual consistency of the results from K07 and B08 can be shown using the background-subtracted 24 $\mu$m, FUV and H$\alpha$ images of M51a, combined with the BIMA SONG CO map. We switch our pixel-by-pixel analysis to 507 pc (adopting a distance of $D$=8.0 Mpc), the scale examined in K07 (520 pc, assuming $D$=8.2 Mpc), to retrieve their results, where OLS bisector fittings are performed again, with the local background subtracted in the SFR map. Our 500 pc molecular-only S-K law in M51a has a slope of $\gamma_{H_2} = 1.48 \pm 0.06$, slightly steeper than but only 1.3$\sigma$ away from what is obtained by K07 through H$\alpha$ + 24 $\mu$m SFR, $\gamma_{H_2,K07} = 1.37 \pm 0.03$. The best-fit power relation between the two SFR tracers is given by SFR$_{FUV+24\ \mu m} \propto$ SFR$_{H\alpha+24\mu m}^{0.95\pm0.01}$. This calibration now has been improved relative to that from the unsubtracted images (section 3.2) by a remarkably weakened scatter at the faint end, and the tight correlation now extends down to SFR $\sim 10^{-4}$ M$_\odot$ yr$^{-1}$ kpc$^{-2}$, implying the applicability of FUV + 24$\mu$m as a SFR tracer as long as the local background is properly removed. Not surprisingly, $\gamma_{H_2}$ changes insignificantly to 1.47±0.05 if unobscured SFRs are measured by substituting H$\alpha$ with FUV luminosity. A even stronger sign of no correlation between $\Sigma_{HI}$ and $\Sigma_{SFR}$ is seen. For the total gas, we find a best-fit $\gamma_H$=1.52±0.05 when a 3-$\sigma$ sensitivity limit cutoff is adopted for the total hydrogen mass surface density, virtually identical to the K07 result. However, from a practical point of view, only those data points with both H I and CO detections above their respective 3$\sigma$ should be taken into account for the linear fit, just as K07 did in their study of total gas surface density scaling relation. Such a criteria results in a steeper slope $\gamma_H$=1.66±0.06, still consistent with K07. Hence, all the results that K07 obtained by performing aperture photometry are reproduced with our pixel-by-pixel analysis on the background subtracted images.

In conclusion, using the same set of data as K07 and B08, our analysis accurately reproduces the results of both investigations. We hereby conclude that at least for the case of M51a, the crux of their discrepancy lies in the preservation/elimination of the local background in 24 $\mu$m, FUV maps and H$\alpha$ images, ruling out the different employed measuring strategies (aperture photometry vs. pixel-by-pixel analysis) and any other factors as possible important causes.

### 4. STAR FORMATION IN M51A AND NGC 3521 ON SUB-KPC SCALES

The BIMA SONG CO map of M51a has been used so far for the purpose of comparison only, and is now replaced with the more recent CARMA + NRO45 data to actually probe the spatially-resolved S-K law. For NGC 3521, the spatial resolution of our data set is limited by that of the H I map (8.19″×6.41″), corresponding to a physical scale of 320 pc at the adopted distance, 8.03 Mpc. However, the resolution limit of molecular-only S-K law can be pushed to smaller scale values, to 220 pc or 5.7″, the PSF FWHM of the 24 $\mu$m image. As for M51a, the similar resolutions of its H I map (5.82″×5.56″) and 24 $\mu$m image set the accessible limit to be $\sim$ 230 pc.

The H I and 24 $\mu$m maps, which have the coarsest pixels (1.5″), define the grid onto which images are registered. We then smooth all the images to make the PSF circular with the same resolution and rescale the pixels to match that resolution before converting flux and surface brightness units to physical quantities. An inclination angle of 72.7° (42°) results in a correction factor of 0.29 (0.74) for projected surface densities in NGC 3521 (M51a). The CO data, having a lower sensitivity limit than H I by a factor of $\sim$2.3, set our limiting sensitivity to the cold gas surface density measurement. Justified by the results of the previous sections, we now apply a pixel-by-pixel analysis to both galaxies, M51a and NGC 3521, utilizing SFR images where the diffuse emission/local background has been removed. The S-K law of M51a and NGC 3521 are shown in Figure 5 and Figure 6 at their highest available resolution, respectively.

We now investigate the scaling relationships at different spatial resolutions. The dependence of best-fit parameters on spatial resolution is shown in Figure 7, where a series of power-law indices for M51a and NGC 3521 are shown in parallel. The range of spatial scales is different for these two objects due to their difference in inclination which yields a factor 2.5 smaller apparent minor axis in NGC 3521 ($\sim$3 kpc across) than in M51a. Investigations on scales larger than a quarter of this length will be of little significance because of the paucity of data points and of including a too large fraction of the galaxy. Moreover, the high inclination of NGC 3521 makes the removal of the background non-star-forming light more complicated, which can affect our results especially on relatively larger scales. Considering the inclination of NGC 3521, 700 pc actually corresponds to a physical scale of $\sim$2 kpc, which we take as a convenient limit for our study. The best-fit parameters of the molecular S-K law in M51a and NGC 3521 at different resolutions are reported in Table 1 and Table 2, where SFR is derived from the weighted sum of H$\alpha$ and 24 $\mu$m luminosities.

Figure 7 demonstrates that $\gamma_{SFR}$ has little dependence on spatial resolution in both galaxies, varying between 0.97 and 1.01 in M51a and between 0.99 and 1.04 in NGC 3521. The weak ascending trend of $\gamma_{SFR}$ is caused by the larger scatter at the faint end as discussed in the methodology section, and the uncertainty in background removal may also play a role. The FUV+24 $\mu$m luminosity is therefore also a good SFR tracer as long as the diffuse emission component is properly removed.

Figure 7 also reveals that the power-law indices of both the molecular and the total hydrogen S-K law decrease monotonically as the spatial scale increases. Specifically, as the resolution decreases from 230 pc to 1 kpc, $\gamma_{H_2}$ decreases from 1.9 to 1.2, implying higher star formation efficiency (defined as the SFR-to-gas surface density ratio) in the denser regime of molecular gas on all sub-kpc but super-GMC scales. For the total gas, we find $\gamma_H$ decreases from 2.1 to 1.6 on the whole range of scales. At $\sim$500 pc resolution, we find steeper slopes ($\gamma_{H_2} \sim 1.5$, $\gamma_H \sim 1.8$) than K07 ($\gamma_{H_2,K07} \sim 1.4$, $\gamma_{H,K07} \sim 1.6$), mainly because the new CARMA + NRO45 data is more sensitive than the BIMA SONG map by a factor of $\sim$2, and has collected more diffuse emission from CO, pushing the low density end to higher values. A even steeper slope would be found if we followed B08, assumed no molecular gas outside the star-forming disk and fit the

scaling relation on the whole isophotal area defined by $D_{25}$.

In contrast to M51a, the high inclination of NGC 3521 results in blending of star formation sites which complicates the removal of diffuse stellar/dust emission, and can affect our result on relatively larger scales. Figure 7 shows that the slopes of the S-K law of both the total and molecular gas and of the SFR indicator comparison for NGC 3521 are less certain and stable than M51a, indicating higher uncertainties in the local background subtraction. In addition, the FoV of our CARMA observation covers only about half of the $D_{25}$ scale, missing the information from the outskirt of the disk where the transition from dominant molecular phase to dominant atomic phase in the cold gas occurs. This shortcoming tends to reduce the amount of data points in the regime slightly denser than $\Sigma_H \sim 10\ M_\odot\ \mathrm{yr}^{-1}\ \mathrm{kpc}^{-2}$ and could have steepened the resulting slope. Bearing in mind these potential issues, we still observe a descending trend similar to that of M51a in both $\gamma_{H_2}$ and $\sigma_{H_2}$. However, both quantities are smaller than in M51a at a given resolution: $\gamma_{H_2}$ is flatter by $\sim 0.3$, and $\sigma_{H_2}$ smaller by $\sim 0.15$. The power-law index of $\gamma_H$ in NGC 3521 fluctuates weakly within the errors and persists between 2.1 and 2.2, implying very weak or no dependence on the resolution. However, as we have mentioned above, this may due to the absence of the CO data in the outer star-forming disk which hinders a complete sampling over the range of gas surface density.

The scatter or dispersion of the S-K law, quantitatively defined as the r.m.s. of the fitting residuals measured perpendicular to the best-fit line, is an important parameter indicating the validity of the S-K law. The study of K07 suggests that the 500-pc-scale total-gas S-K law has a scatter almost twice as large of the 2-kpc-scale measurements in M51a, which becomes the first hint of the existence of some scale below which the total-gas S-K law breaks down. Figure 7-b reveals the monotonic decreasing trend of the scatter ($\sigma_{H_2}$) about the best-fit molecular S-K law as the resolution becomes lower on sub-kpc scales in both our program galaxies. Momose et al. (2010) analysed the CARMA + NRO45 CO data of NGC 4303 and find that the K-S law already breaks down at $\sim 250$ pc resolution, and does not recover unless the data are smoothed to a scale of 500 pc or larger, especially in the disk region of the galaxy. Conversely, Verley et al. (2010) show that a loosely correlated total S-K law exists down to 180 pc in M33 (0.84 Mpc), and Onodera et al. (2010) conclude that the S-K law of $H_2$ in M33 becomes invalid only at the scale of GMCs ($\sim 80$ pc). Limited by the angular resolution, we are unable to reach scales below $\sim 200$ pc, but significant scatter ($\sigma_{H_2}$=0.62 dex for M51a and 0.52 dex for NGC 3521) about the best-fit molecular S-K law is observed in both galaxies at their highest available resolution. When the linear size increases by a factor of 3 ($\sim 700$ pc), the scatter decreases to 0.48 (M51a) and 0.26 dex (NGC 3521). Assuming the trend in Figure 7 [b] extends to smaller scales, a rough extrapolation gives a scatter of close to 0.7 dex at 80 pc scale, enough to mask any trend. The smoothly increasing scatter suggests the absence of a *characteristic* breakdown scale of the S-K law, but the scaling relationship will be overcome by the large scatter gradually. Higher resolution datasets are required to definitively pin

down this issue.

As an exploratory experiment, we also attempt to find a common formulation that relates the observational results in the two galaxies, so that some hints for the underlying physical universality may be obtained. Since the molecular S-K law is what should be focused on on sub-galactic scales, $\gamma_{H_2}$ is of interest in the first place. Furthermore, because the uncertainty in the photometric measurements is typically at the level of $\sim 10$–20%, the dispersion about the best-fit S-K law is mainly intrinsic, as has been pointed out by previous studies (K07; Blanc et al. 2009), and $\sigma_{H_2}$ is a quantity of physical importance.

The uncertainties of the slopes $\gamma_{H_2}$ in Tables 1 and 2 are, in fact, fitting errors, and are consistent in value with those already reported in the literature (K07; Blanc et al. 2009). These uncertainties are not fully related to the dispersions $\sigma_{H_2}$, since, for instance, a larger dynamical range on the data could decrease the slope uncertainty, even at constant $\sigma_{H_2}$. Hence the relevance of the intrinsic data scatter $\sigma_{H_2}$, which we report as separate columns in Tables 1 and 2.

As mentioned above, $\gamma_{H_2}$ and $\sigma_{H_2}$ are systematically smaller in NGC 3521 than in M51a. However, the resolution under consideration is the *projected* scale, and the comparison between the two galaxies should be made on the basis of *physical* or *de-projected* scales. We hence re-plot the dependence of $\gamma_{H_2}$ and $\sigma_{H_2}$ on $\delta_{dp}$ ($\equiv \delta / \cos\ i$) in Figure 8. As revealed by the two panels, on sub-kpc but super-GMC scales, both quantities are surprisingly consistent between the two galaxies. This remarkable result is a sign that we are approaching the scale where the physical origin of the S-K law is appearing. We are motivated to propose the following relations which hold in both galaxies:

$$\gamma_{H_2} = A\ \log\ [\delta_{dp}/\mathrm{kpc}] + B, \qquad (6)$$

and

$$\sigma_{H_2} = C\ [\delta_{dp}/\mathrm{kpc}] + D, \qquad (7)$$

where $\sigma_{H_2}$ is in dex, and $A = -1.09 \pm 0.05$, $B = 1.36 \pm 0.02$, $C = -0.19 \pm 0.01$ and $D = 0.67 \pm 0.01$. These best-fit parameters are determined using the data of M51a only, which are superior than those of NGC 3521 in many respects, as explained above. The values change minimally if the latter is included in the fits because of the impressive overlap among the data (Figure 8). This overlap seemingly indicates a universal sub-kpc molecular S-K law that persists amongst spiral galaxies whose actual form depends only on the physical scale being considered. An extrapolation of the above expression for $\gamma_{H_2}$ shows that a slope of unity requires a scale as large as $\sim 2$ kpc, roughly the typical spacing of adjacent spiral arms in disk galaxies similar to M51a and NGC 3521. This has been verified in NGC 3521 (Figure 7-a), where $\gamma_{H_2}$ is consistent with unity within the error bars at the apparent scale $\delta \sim 700$ pc (Table 2), which corresponds to a de-projected scale $\delta_{dp} \sim 2$ kpc.

Similarly, we find that the $\gamma_H - \delta$ correlation in M51a can be fitted to

$$\gamma_H = -0.88\ \log\ [\delta/\mathrm{kpc}] + 1.60.$$

For a projected scale $\delta$=1.80 kpc (corresponding to 1.85 kpc if $D$=8.2 Mpc is adopted as in K07), the extrapola-

tion of the above function predicts $\gamma_H$=1.36, well consistent with the slope $1.37 \pm 0.03$ found at this resolution by K07 for the total hydrogen S-K law using the 14-m Five College Radio Astronomical Observatory CO ($J$=1–0) map (Lord & Young 1990). Despite this consistency, we are aware of the uncertainties in deriving large scale information from the extrapolation of our sub-kpc study.

The discussion above leads to a conclusion that caution must be taken in interpreting observational results, especially those of galaxies with high inclinations, which makes the intended sub-kpc studies actually "super-kpc". Linear or sub-linear molecular S-K laws may be found if spiral structures are not readily resolved. The HERACLES CO ($J$=2–1) data that is used by B08 has a resolution of $11''$ (Leroy et al. 2009). This spatial resolution (430 pc at a distance of 8.03 Mpc where NGC 3521 is located, or 570 pc at 10.7 Mpc adopted by B08) translates to $\delta_{dp} \sim 1.5$ kpc, already close to the $\sim 2$ kpc unity-slope scale, and is virtually incapable of resolving the spiral structure of NGC 3521, which is likely to be another important reason for the results in B08 in addition to preserving the local background in the SFR measurements.

At our highest available physical resolution ($\delta_{dp}$=320 pc) in M51a, the power indices of both the molecular and total hydrogen S-K laws are about 2 ($\gamma_{H_2} = 1.91 \pm 0.03$, $\gamma_H = 2.14 \pm 0.04$). A slope as steep has never been reached in spatially-resolved studies of extragalactic star-forming disks, but has been observed inside the Milky Way. For instance, Misiriotis et al. (2006) derive both the gas/dust distribution and SFR from COBE/DIRBE data and find $\gamma_H = 2.18 \pm 0.20$; Gutermuth et al. (2011) directly observed about 7000 young stellar objects (YSOs) and obtain a slope $\sim 2$, where the gas density is traced by dust extinction. Our results in M51a are therefore very similar to these Galactic investigations, which seems to hint at an "intrinsic" S-K law with slope $\sim 2$ in spiral galaxies, and the flatter power indices that have been found in other galaxies are actually a resolution effect. As a minimum, we have added evidence that a super-linear relation is found in extragalactic investigations supporting the recent results that the star formation efficiency positively correlates with the column density for Galactic molecular clouds (Gutermuth et al. 2011). As a caveat, our study has been performed only on two galaxies, and more data with better sensitivity, resolution and broader FoV for a larger sample of galaxies are required to confirm the results presented in this section.

## 5. DISCUSSION

### 5.1. The Nature of the Diffuse Emission at all Wavelengths

Among the SFR images, the extended background contamination is the most significant at 24 $\mu$m. Popescu et al. (2005) find that the IR-to-UV ratio is higher in the interarm regions of M101 than the arm regions, which they interpret as due to dust heated by optical photons in the interstellar radiation field. In order to account for the observed SEDs of dust emission, a dust model must include a substantial population of ultrasmall grains or large molecules with the vibrational properties of PAH material and with sizes such

that single-photon heating can excite the observed vibrational emission (Draine & Li 2007). Therefore, the mid-IR emission is produced not only by dust grains heated by young stellar populations, but also, and in some areas predominantly, by dust heated by older stars through single-photon processes (e.g., Draine & Li 2007). The latter component is unassociated with current star formation, and is likely to dominate the mid-IR emission in the faint, diffuse regions in galaxies. As a quantification of the amount of diffuse light at each position in the two galaxies, we show in Figure 9 the ratio of the compact (background-subtracted) emission to the diffuse component (the subtracted background) in H$\alpha$, 24 $\mu$m and FUV as a function of H$_2$ mass surface density at 400 pc resolution (projected scale). It can be seen that, among the three wavelengths, the 24 $\mu$m emission shows the most marked trend for increasing compact-to-diffuse ratio with increasing $\Sigma_{H_2}$ (especially in M51a). The variation of the compact-to-diffuse ratio is broader at 24 $\mu$m than H$\alpha$ and FUV (especially in M51a), in line with the strongest influence from its diffuse emission. In general, the fact that young stars form in dusty galactic environment leads often to the prevalence of dust-obscured SFR (traced by IR) over unobscured SFR (traced by optical and UV), implying that the slope of the S-K law is mainly driven by the way the diffuse 24 $\mu$m emission is handled.

In the FUV data, the diffuse component is also considerably stronger than in the H$\alpha$ images (Meurer et al. 1995; Maoz et al. 1996), likely owing to the longer timescale over which UV continuum photons can be produced. As an example, it takes only 9 Myr for the H$\alpha$ emission of an instantaneous-burst population to diminish by two orders of magnitude, but takes about 100 Myr at 1500 Å where the FUV band of GALEX resides (Leitherer et al. 1999). As a result of galaxy dynamics, over 100 Myr, the UV-emitting stars will have migrated away from their birth-site, and will have diffused across the galactic disk over an area at least 10 times larger than that of the ionizing-photon-emitting stars (Chandar et al. 2005; Pellerin et al. 2007). This results in a vastly reduced contrast between the arm and inter-arm regions of galaxies in FUV ($\sim$15:1 in M51a after extinction correction) relative to the H$\alpha$ (>30:1 in M51a), and also in a less obvious association between the location of the FUV emission and present-day star formation. Investigations on the properties of diffuse UV emission have demonstrated that, the diffuse UV light is likely originating from evolved, disrupted stellar clusters that has migrated away from their birth-sites (Tremonti et al. 2001; Chandar et al. 2005); any assumptions of in-situ star formation for the diffuse UV light implies a steep IMF which is either steeper than Kroupa at the high mass end ($\gtrsim$10-20 $M_\odot$) or truncated (down to 30-40 $M_\odot$) (e.g., Tremonti et al. 2001).

To estimate the impact of the diffuse UV light, we assume that star formation proceeds at a roughly constant rate over 1 Gyr, and that stars and molecular clouds remain closely associated over $\sim$30 Myr (Blitz & Shu 1980; Elmegreen 2007), in agreement with some observations for the oldest stars found in GMCs (Oliveira et al. 2009). Stellar population synthesis models (STARBURST99, Leitherer et al. 1999) indicate that for constant star formation, 80% of the GALEX FUV light is

produced by stars younger than 30 Myr, and 20% by stars older than 30 Myr. If the older stars get dispersed over the galactic disk, their mean dust attenuation will be lower than that of the younger stars, which are clustered in the spiral arms. Using the opacity values of Holwerda et al. (2005), $A_{I,\mathrm{arm}} \sim 1.5$ mag and $A_{I,\mathrm{interarm}} \sim 0.5$ mag, and the conservative assumption of a mixed dust/star geometry, with a Milky Way extinction curve plus albedo (Calzetti et al. 1994, 2000), the contribution to the total *observed* FUV emission of a galaxy from stellar populations younger than 30 Myr is only about 60%. Other assumptions for the dust/star geometry and the effective attenuation will lead to smaller fractions contributed by the young star populations to the total observed FUV. In light of the above modeling, unless stellar populations significantly older than 30 Myr remain closely associated to their birth cloud, at least a 40% fraction of "diffuse" UV light should be present. Our strategy of diffuse emission subtraction presented here results in an observationally determined diffuse FUV fraction of 44% in M51a and 53% in NGC 3521. By virtue of its lower inclination, M51a has a more reliable measurement, and our modeling and observation are therefore consistent.

Although removing the diffuse FUV emission is clearly a necessity for measuring SFRs, we have performed a test by making a SFR map of M51a with local background *preserved* for the FUV image but *subtracted* for 24 $\mu$m. Compared to our fiducial method of SFR tracing (H$\alpha$+24$\mu$m with the background removed in both bands), this SFR map reduces the slope of the molecular S-K law $\gamma_{H_2}$ from 1.42±0.05 to 1.14±0.04 at 750 pc resolution, higher than the slope 0.83±0.04 obtained when both the FUV and 24 $\mu$m backgrounds are preserved. Thus, keeping the FUV background recovers a slope roughly half-way between those obtained when either removing or preserving both backgrounds. However, we still recover non-linear trends at high spatial resolution: $\gamma_{H_2}$=1.39±0.02 at 250 pc resolution, when preserving the FUV background and removing it from the 24 $\mu$m image, to be compared with $\gamma_{H_2}$=1.86±0.03, when the background is removed from both images.

The stronger diffuse emission in UV relative to the H$\alpha$ is the underlying reason for the deviation of the SFR$_{\mathrm{FUV}+24\mu m}$ vs. SFR$_{\mathrm{H}\alpha+24\mu m}$ correlation from a single power law at the faint end (see Figure 4-c). As we have shown, this deviation can be calibrated by careful local background removal, whose necessity is thus justified by the need to include in our SFR indicators only the young stellar populations (and the dust they heat) involved in the *current* star formation activity. By including the local background contamination in their SFR estimates, B08 systematically overestimates the current SFRs at the faint end, which affects the physical interpretations of their high quality observations.

The H$\alpha$ data are processed with our strategy as well, driven by the fact that a fraction of ionizing photons escape from H II regions and result in the diffuse emission from ambient ionized gas unrelated to the current star formation at a specific location (Ferguson et al. 1996, 1998; Wang et al. 1999; Heckman et al. 1999). Another reason is that pixel-by-pixel analysis is highly sensitive to the low level uncertainty in flat-fielding, continuum subtraction and sky background removal and requires careful

handling. In fact, this technical difficulty can be circumvented by using integral field spectroscopy, as is done by Blanc et al. (2009). The authors investigated the central $4\times4$ kpc$^2$ of M51a at 170 pc resolution, with the diffuse H$\alpha$ emission corrected based on [S II]/H$\alpha$ line ratio, as an alternative to the local background removal in K07 and our work. Combining these data and the archival BIMA SONG CO map, they fit the data through a Monte Carlo approach with upper limits included and find a sub-linear slope $\gamma_{H_2} = 0.82 \pm 0.05$ for the molecular S-K law, similar to 0.84 obtained by B08. However, as they have pointed out, when an ordinary least-square (OLS) bisector linear fitting excluding upper limits (as throughout this paper, K07 and B08) is performed on their data, the slope steepens to 1.5, close to $\sim1.4$ found by K07. At our highest available resolution (230 pc) when the same BIMA SONG map is used, we find a similar power index $1.45 \pm 0.03$ if we only exclude all data points with significance below $1\sigma$ as Blanc et al. (2009) did, rather than our default $3\sigma$. Hence, they actually reach a conclusion consistent with K07 and this study, when noisy (below $1\sigma$) CO data are removed from their analysis.

## 5.2. *Robustness Tests*

In this work, we have performed our analysis in a customary manner, i.e. by working above a certain sensitivity threshold (3-$\sigma$). Blanc et al. (2009) simulate the likely distribution of non-detections so that data below 1-$\sigma$ detection limits can be included in their power-law fitting. While this approach attempts to avoid data censoring, their strategy requires extremely accurate understanding and reliable modeling of the noise characteristics, which is a challenging enterprise especially for CO maps. Unfortunately, the current major limitation to spatially-resolved S-K law studies is the relatively low sensitivity of the CO maps, and the real solution hinges on the higher quality of future CO data (through, e.g. ALMA). Our CARMA + NRO45 data for M51a is more sensitive than the BIMA SONG map that Blanc et al. (2009) used by a factor of $\sim2$, and has higher image fidelity. Figure 2 compares these two maps at 230 pc scale (corresponding to the BIMA SONG resolution), and demonstrates that the CARMA + NRO45 observations recover slightly more flux at the faint end. Therefore, although different fitting techniques are at play, we have probed the CO emission to the same depth as Blanc et al. (2009), but at a much higher confidence level ($2\sigma$ vs. $1\sigma$).

We now investigate the impact of imposing threshold values to our gas maps. As can be seen in Figures 4-6, the 3-$\sigma$ threshold has negligible impact on the SFR maps. In fact, varying the SFR threshold from $2\sigma$ to $4\sigma$ changes the best-fit slopes minimally (within 0.03). This remains true at all scales. Most of the data censoring occurs on the gas maps. We test the reliability of our fits by varying the CO map threshold from $1\sigma$ to $5\sigma$, and the results are tabulated in Table 3 and Table 4. As can be seen from the various columns, decreasing the threshold of the CO map flattens the slope $\gamma_{H_2}$ at all scales, suggesting that the inclusion of noisy data has adverse effect on the determination of the S-K law. With future deeper CO maps, our current 1-$\sigma$ limits may become better detected, and enable a more accurate determination of the slope of the S-K Law at low CO masses. Using our current well

detected data, with thresholds 3-$\sigma$ or higher, the slope of the molecular S-K law is clearly super-linear.

Finally, one should be aware of the fact that because brightnesses at different wavelengths will often tend to correlate, causal relationships may be masked. In this work, this *richness effect* has been alleviated significantly when the underlying diffuse emission from dust and stars has been removed, and is thus of much less importance than in the study of B08 (one may notice from Figure 3 that the background-subtracted images no longer appear disk-like). The absence of a clear correlation between SFR and atomic hydrogen (especially when the local background component is subtracted, see Figure 4-d) is an implication that our analyses are not dominated by this effect.

Further progress on this problem of how to measure SFRs *locally* within galaxies will require a careful modeling of the diffusion timescales of stellar populations in galaxies as they age, and the analysis of both the direct stellar light (UV, H$\alpha$) and the dust-reprocessed light (IR) from these evolving populations.

## 6. SUMMARY

We have presented a case study of the sub-kpc Schmidt-Kennicutt law of star formation in two nearby galaxies, M51a (NGC 5194) and NGC 3521, using our new CARMA + NRO45 combined CO ($J$=1–0) maps of both galaxies with archival SINGS H$\alpha$, 24 $\mu$m, THINGS H I and GALEX FUV data. Employing a new approach of local background determination, we use the same data sets as Kennicutt et al. (2007) and Bigiel et al. (2008) and quantitatively show that the contrasting results of the two studies on whether the molecular S-K law is super-linear or linear is a result of removing or preserving the local background, this being the sum of the diffuse emission in galaxy disks and bulges from stars and dust. We argue that in order to plausibly derive SFR maps of nearby galaxies, the local mid-IR and FUV background should be subtracted carefully, in order to isolate the currently star-forming regions.

Applying this strategy, we perform a pixel-by-pixel analysis on different physical scales and find the power index of molecular S-K law ($\gamma_{H_2}$) to have similar behavior in these two galaxies. It is super-linear ($\gtrsim 1.5$) at the highest available resolution ($\sim$220 pc), and decreases monotonically as the resolution becomes lower. We also find in both galaxies that the scatter of the molecular S-K law $\sigma_{H_2}$ monotonically increases as the resolution becomes higher, indicating a trend for which the S-K law breaks down below some scale simply by reaching a scatter as large as the trend to be measured. Both $\gamma_{H_2}$ and $\sigma_{H_2}$ are systematically larger in M51a than in NGC 3521. However, when plotted against the *de-projected* scale, both quantities become impressively consistent between the two galaxies, tentatively suggesting that the measured molecular S-K law in spiral galaxies may depend only on the size of the physical scale considered, but does not vary from galaxy to galaxy.

REFERENCES

Bianchi, L., Madore, B., Thilker, D., Gil de Paz, A., & GALEX Science Team 2003, Bulletin of the American Astronomical Society, 35, 1354

Bianchi, L., Madore, B., Thilker, D., Gil de Paz, A., Martin, C., & The GALEX Team 2003, The Local Group as an Astrophysical Laboratory, 10

Bigiel, F. et al. 2008, AJ, 136, 2846

Blanc, G. A., Heiderman, A., Gebhardt, K., Evans, N. J., & Adams, J. 2009, ApJ, 704, 842

Blitz L. 1993. Protostars and Planets III, ed. E Levy, JI Lunine, TM Bania, p. 125. Tucson: Univ. Ariz. Press

Blitz, L. & Rosolowsky, E. 2006, ApJ, 650, 933

Blitz, L., & Shu, F. H. 1980, ApJ, 238, 148

Bloemen, J. B. G. M., et al. 1986, A&A, 154, 25

Boissier, S., Prantzos, N., Boselli, A., & Gavazzi, G. 2003, MNRAS, 346, 1215

Bresolin, F., Garnett, D. R., & Kennicutt, R. C., Jr. 2004, ApJ, 615, 228

Calzetti, D., Kinney, A. L., & Storchi-Bergmann, T. 1994, ApJ, 429, 582

Calzetti, D., Armus, L., Bohlin, R. C., Kinney, A. L., Koornneef, J., Storchi-Bergmann, T., 2000, ApJ, 533, 682

Calzetti, D., Kennicutt, R. C., Bianchi, L., Thilker, D. A., Dale, D. A., Engelbracht, C. W., Leitherer, C., Meyer, M. J., et al. 2005, ApJ, 633, 871

Calzetti, D. et al. 2007, ApJ, 666, 870

Calzetti, D., Sheth, K., Churchwell, E., & Jackson, J. 2009, The Evolving ISM in the Milky Way and Nearby Galaxies

Calzetti, D., et al. 2010, ApJ, 714, 1256

Chandar, R., Leitherer, C., Tremonti, C. A., Calzetti, D., Aloisi, A., Meurer, G. R., & de Mello, D. 2005, ApJ, 628, 210

Dale, D. A., et al. 2005, ApJ, 633, 857

Dale, D. A., et al. 2009, ApJ, 703, 517

Draine, B. T., & Li, A. 2007, ApJ, 657, 810

de Blok, W. J. G., Walter, F., Brinks, E., Trachternach, C., Oh, S.-H., & Kennicutt, R. C. 2008, AJ, 136, 2648

de Vaucouleurs, G., de Vaucouleurs, A., Corwin, H. G., Buta, R. J., Paturel, G., Fouque, P., 1991, Third Reference Catalogue of Bright Galaxies, Vols 13. Springer-Verlag, Berlin, Heidelberg, New York

Elmegreen, B. G. 2002, ApJ, 577, 206

Elmegreen, B. G. 2007, ApJ, 668, 1064

Ferguson, A. M. N., Wyse, R. F. G., Gallagher, J. S., III, & Hunter, D. A. 1996, AJ, 111, 2265

Ferguson, A. M. N., Wyse, R. F. G., Gallagher, J. S., III, & Hunter, D. A. 1998, ApJ, 506, L19

Gnedin, N. Y., Tassis, K., & Kravtsov, A. V. 2009, ApJ, 697, 55

Gordon, K. D., et al. 2004, ApJS, 154, 215

Greenawalt, B., Walterbos, R. A. M., Thilker, D., & Hoopes, C. G. 1998, ApJ, 506, 135

Gutermuth, R. A., Pipher, J. L., Megeath, S. T., Allen, T., Myers, P. C., Allen, L. E., Yergatian, C., & Fazio, G. G. 2011, ApJ, submitted

Heckman, T. M., Armus, L., Weaver, K. A., & Wang, J. 1999, ApJ, 517, 130

Helfer, T.T., Thornley, M.D., Regan, M.W., Wong, T., Sheth, K., Vogel, S.N., Blitz, L., & Bock, D.C.-J. 2003, ApJS, 145, 259

Heyer, M. H., Corbelli, E., Schneider, S. E., & Young, J. S. 2004, ApJ, 602, 723

Holwerda, B., Gonzalez, R. A., Allen, R. J., & van der Kruit, P. C. 2005, AJ, 129, 1396

Hunter, D. A., Elmegreen, B. G., & Baker, A. L. 1998, ApJ, 493, 595

Isobe, T., Feigelson, E. D., Akritas, M. G., & Babu, G. J. 1990, ApJ, 364, 104

Karachentsev, I. D., Karachentseva, V. E., Huchtmeier, W. K., & Makarov, D. I. 2004, AJ, 127, 2031

Kennicutt, R. C., Jr. 1989, ApJ, 344, 685

Kennicutt, R.C. 1998, ARA&A, 36, 189

Kennicutt, R. C., Jr., et al. 2003, PASP, 115, 928

Kennicutt, R. C., Jr., et al. 2007, ApJ, 671, 333

Kennicutt, R. C., Jr., Lee, J. C., Funes, S. J., José G., Sakai, S., & Akiyama, S. 2008, ApJS, 178, 247

Koda, J., Sawada, T., Hasegawa, T., & Scoville, N. Z. 2006, ApJ, 638, 191

Koda, J., & the Nearby Galaxies CO Survey Group 2009b, AAS, 213, 485.04

Koda, J., et al. 2009a, ApJ, 700, L132

Koda, J., et al. 2011, ApJS, 193, 19

Kroupa, P., 2001, MNRAS, 322, 231

Krumholz, M. R., McKee, C. F., & Tumlinson, J. 2009, ApJ, 699, 850

Lee, J. C., et al. 2009, ApJ, 706, 599

Leitherer, C., et al. 1999, ApJS, 123, 3

Leroy, A. K., Walter, F., Brinks, E., Bigiel, F., de Blok, W. J. G., Madore, B., & Thornley, M. D. 2008, AJ, 136, 2782

Leroy, A. K. et al. 2009, AJ,, 137, 4670

Liu, G., Calzetti, D., Kennicutt, R. C., Jr., Schinnerer, E., Sofue, Y., Komugi, S., & Egusa, F., 2011, in preparation

Lord, S. D., & Young, J. S. 1990, ApJ, 356, 135

Madsen, G. J., Reynolds, R. J., & Haffner, L. M. 2006, ApJ, 652, 401

Maoz, D., Barth, A. J., Sternberg, A., Filippenko, A. V., Ho, L. C., Macchetto, F. D., Rix, H.-W., & Schneider, D. P. 1996, AJ, 111, 2248

McKee, C. F., & Ostriker, E. C. 2007, ARA&A, 45, 565

Meurer, G. R., Heckman, T. M., Leitherer, C., Kinney, A., Robert, C., & Garnett, D. R. 1995, AJ, 110, 2665

Misiriotis, A., Xilouris, E. M., Papamastorakis, J., Boumis, P., & Goudis, C. D. 2006, A&A, 459, 113

Momose, R., Okumura, S. K., Koda, J., & Sawada, T. 2010, ApJ, 721, 383

Moustakas, J., Kennicutt, R. C., Tremonti, C. A., Dale, D. A., Smith, J.-D. T., & Calzetti, D. 2010, ApJS, 190, 233

Oliveira, I., Merin, B., Pontoppidan, K. M., et al. 2009, ApJ, 691, 672

Onodera, S., et al. 2010, ApJ, 722, L127

Osterbrock, D.E. & Ferland, G.J. 2006, Astrophysics of Gaseous Nebulae and Active Galactic Nuclei, 2nd. ed. (Sausalito, CA: Univ. Science Books)

Pellerin, A., Meyer, M., Harris, J., & Calzetti, D. 2007, ApJ, 658, L87

Popescu, C. C., et al. 2005, ApJ, 619, L75

Sault, R. J., Teuben, P. J., & Wright, M. C. H. 1995, Astronomical Data Analysis Software and Systems IV, 77, 433

Sawada, T., et al. 2008, PASJ, 60, 445

Schaerer, D., & de Koter, A. 1997, A&A, 322, 598

Schmidt, M. 1959, ApJ, 129, 243

Scoville, N.Z. et al. 2001, AJ, 122, 3017

Tamburro, D., Rix, H.-W., Walter, F., Brinks, E., de Blok, W. J. G., Kennicutt, R. C., & Mac Low, M.-M. 2008, AJ, 136, 2872

Tan, J. C. 2010, ApJ, 710, L88

Tasker, E. J., & Tan, J. C. 2009, ApJ, 700, 358

Thilker, D.A., Braun, R., & Walterbos, R.A.M. 2000, AJ, 120, 3070

Thornley, M. D. 1996, ApJ, 469, L45

Tremonti, C. A., Calzetti, D., Leitherer, C., & Heckman, T. M. 2001, ApJ, 555, 322

Verley, S., Corbelli, E., Giovanardi, C., & Hunt, L. K. 2010, A&A, 510, A64

Walter, F., Brinks, E., de Blok, W. J. G., Bigiel, F., Kennicutt, R. C., Thornley, M. D., & Leroy, A. 2008, AJ, 136, 2563

Wang, J., Heckman, T. M., & Lehnert, M. D. 1999, ApJ, 515, 97

Wong, T., & Blitz, L. 2002, ApJ, 569, 157

Wyse, R. F. G., & Silk, J. 1989, ApJ, 339, 700

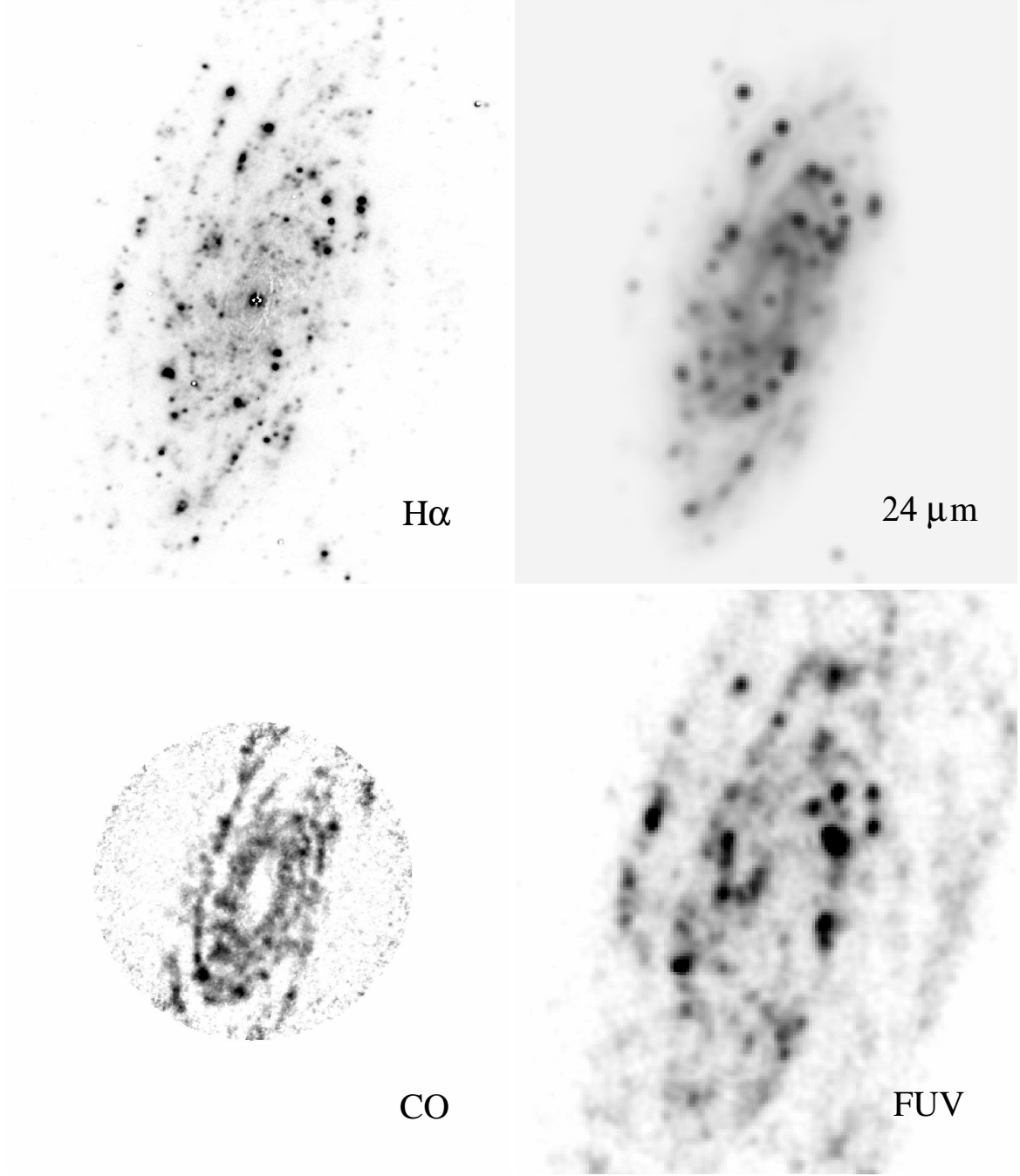Fɪɢ. 1.— The KPNO 2.1-m Hα, Spitzer MIPS 24 μm, CARMA CO (J=1–0) and GALEX FUV images of NGC 3521. North is up, East is left. The scale of each panel is 4.0′ × 4.6′, corresponding to 9.3×10.7 kpc².
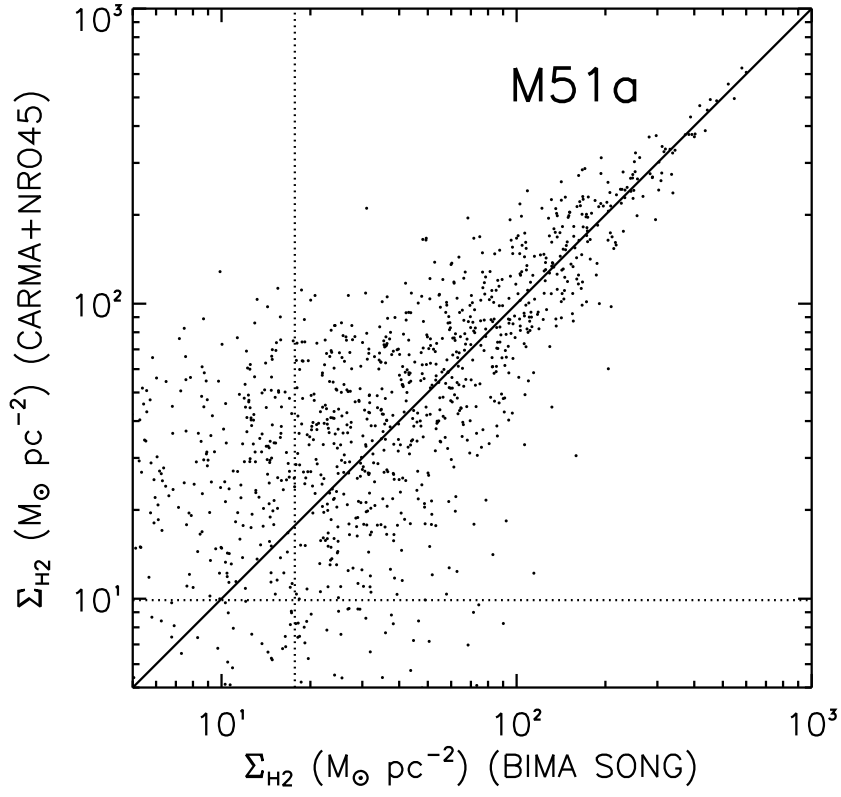
FIG. 2.— Comparison of calculated molecular hydrogen surface densities in M51a between our CARMA + NRO45 and BIMA SONG CO measurements at the 230 pc (5.8″) resolution. The 3-$\sigma$ sensitivity limits of the SONG and our data at this resolution (18 and 9.9 $M_\odot$ pc$^{-2}$, respectively) are indicated by the dotted lines. The solid line indicates the expected unit slope in the case of perfect consistency. It is seen that the new CARMA + NRO45 data recover more CO flux at the faint end, and is deeper by a factor of $\sim$2 than the BIMA SONG data.
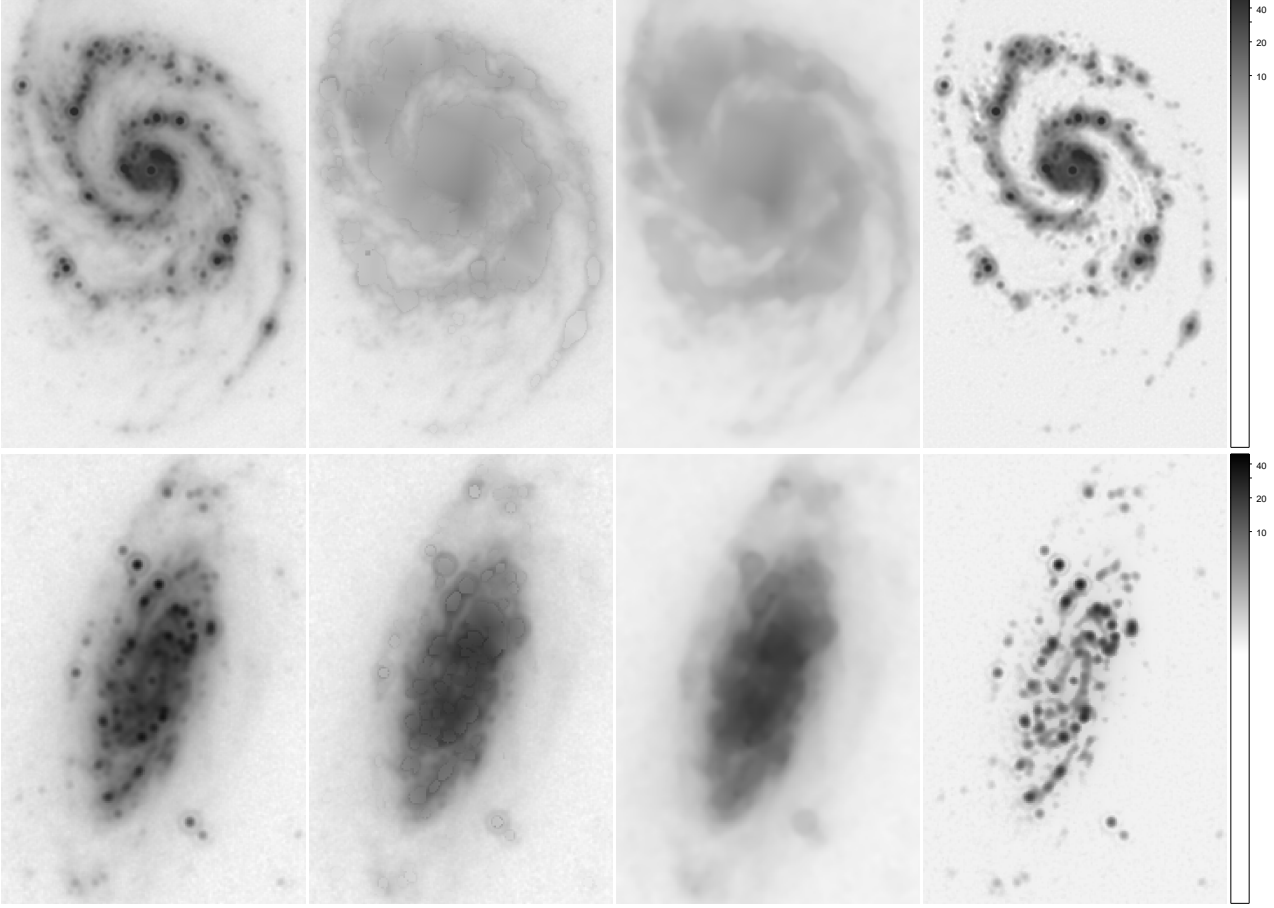
Fig. 3.— The products of our local background removal strategy applied on the 24 $\mu$m images of M51a (top row) and NGC 3521 (bottom row). In each row, the compact emission component of the original image (first column) is identified and removed by adopting the algorithm of *HIIphot*, then the resultant image (second column) is smoothed by replacing each pixel with the median of a moving box so that no sharp features exist. The background image is thus created (third column) and subtracted from the original image, so that the final background-free image (last column) is prepared for our analysis. All images for each galaxy share common logarithmetic grey scales displaying surface brightness in units of MJy sr$^{-1}$.

FIG. 4.— The correlations for M51a between derived physical quantities at 750 pc resolution (at a distance of 8.00 Mpc). For the left panel in each pair the local backgrounds in the Hα, 24 μm and FUV images are not removed (denoted by "BG+"), but are removed in the right panel ("BG−"). The fitted slopes are indicated at the bottom-right of each panel. [a] the molecular-only S-K law with SFR derived from Hα+24 μm; [b] the molecular-only S-K law with SFR derived from FUV+24 μm; [c] the correlation between SFRs derived from Hα+24 μm and FUV+24 μm, respectively; [d] the relation of Hα+24 μm SFR vs. H I surface density; [e] the total hydrogen S-K law with SFR derived from Hα+24 μm; [f] the total hydrogen S-K law with SFR derived from FUV+24 μm. In each panel, the horizontal and vertical dotted lines locate the 3-$\sigma$ sensitivity limit of the two involved quantities. Note that in general, the sensitivity limit of $\Sigma_{\rm SFR}$ is not the limiting factor for our fitted range, while $\Sigma_{\rm gas}$ is. Those data points with sufficient S/N ratio for linear bisector fittings are shown as solid black dots, in contrast to the low S/N light grey dots. In panel [e], the solid line corresponds to the fit using points where CO, H I and SFR are independently above 3$\sigma$ (best-fit power index $\gamma_{\rm H} = 1.63 \pm 0.08$), while the dashed line results from requiring the total hydrogen surface density and SFR to be above 3$\sigma$ (best-fit $\gamma_{\rm H} = 1.42 \pm 0.06$).
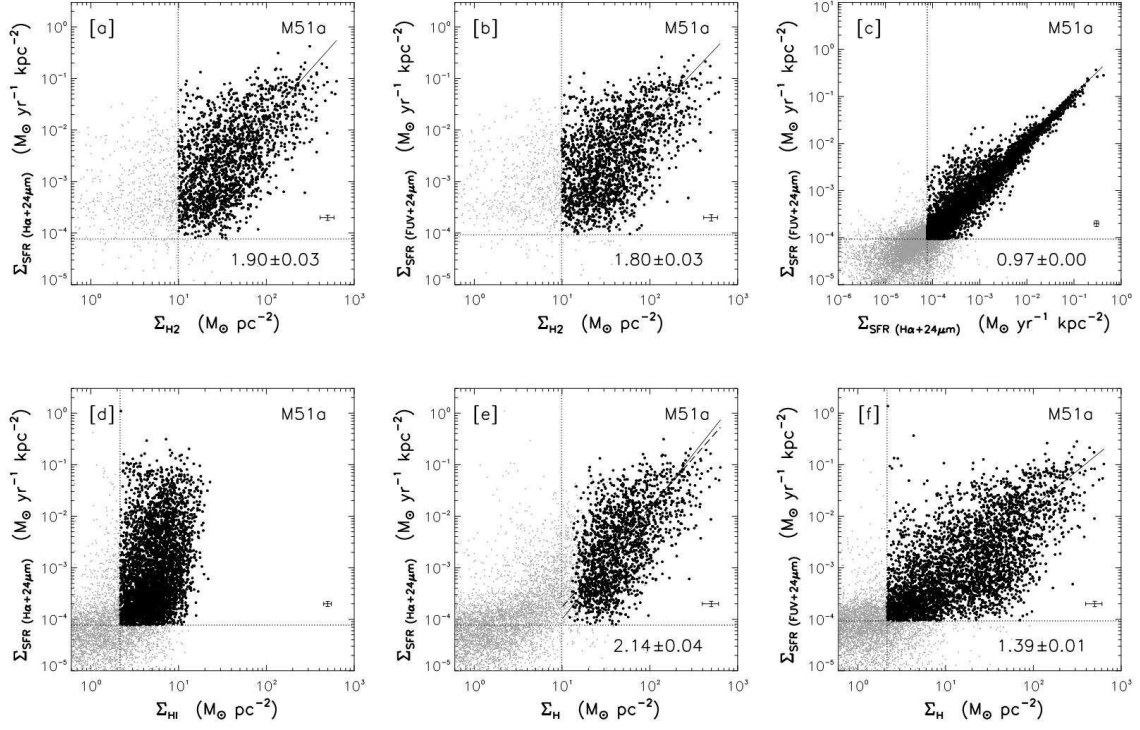
FIG. 5.— The scaling relations of star formation for M51a at the highest available resolution (230 pc). The local backgrounds in Hα, 24 μm and FUV images have been removed, following our strategy. The symbols, notes and involved physical quantities are identical to Figure 4.
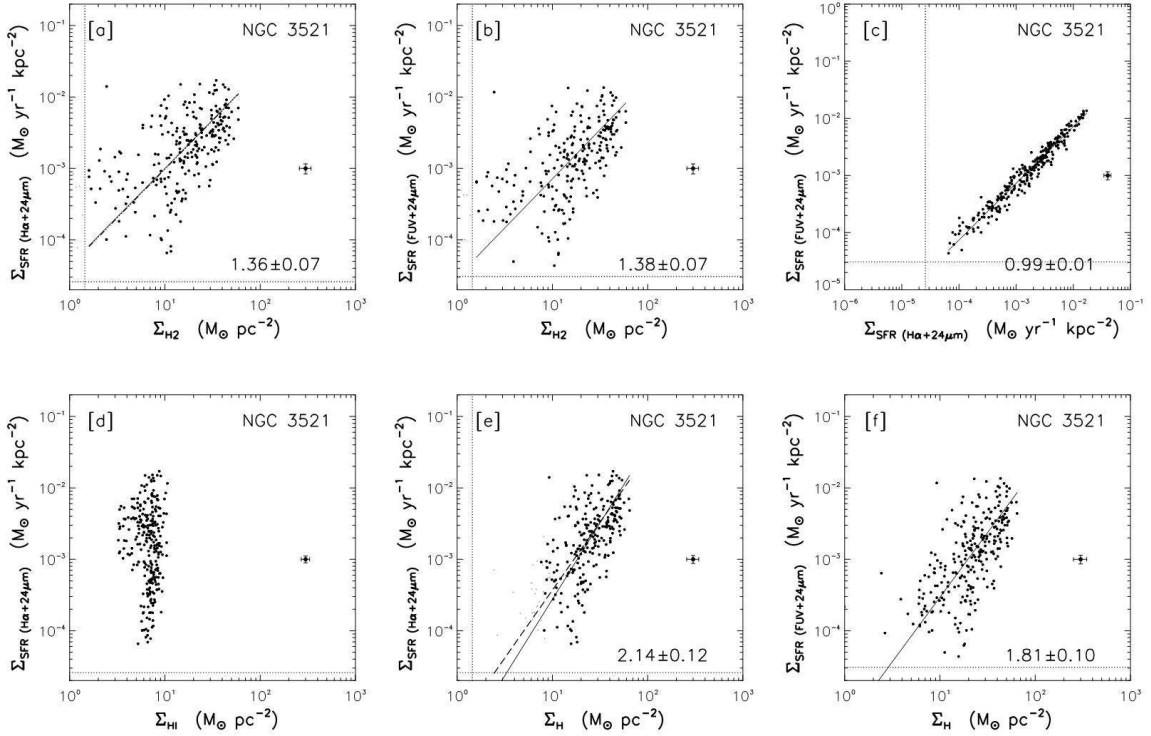


FIG. 6.— The scaling relations of star formation for NGC 3521 at the highest available resolution for H I data (320 pc). The local backgrounds in Hα, 24 μm and FUV images have been removed, following our strategy. The symbols, notes and involved physical quantities are identical to Figure 4. All quantities are compared inside the FoV of CARMA CO data, which is ∼ 30% of the optical area defined by $D_{25}$ used by B08.
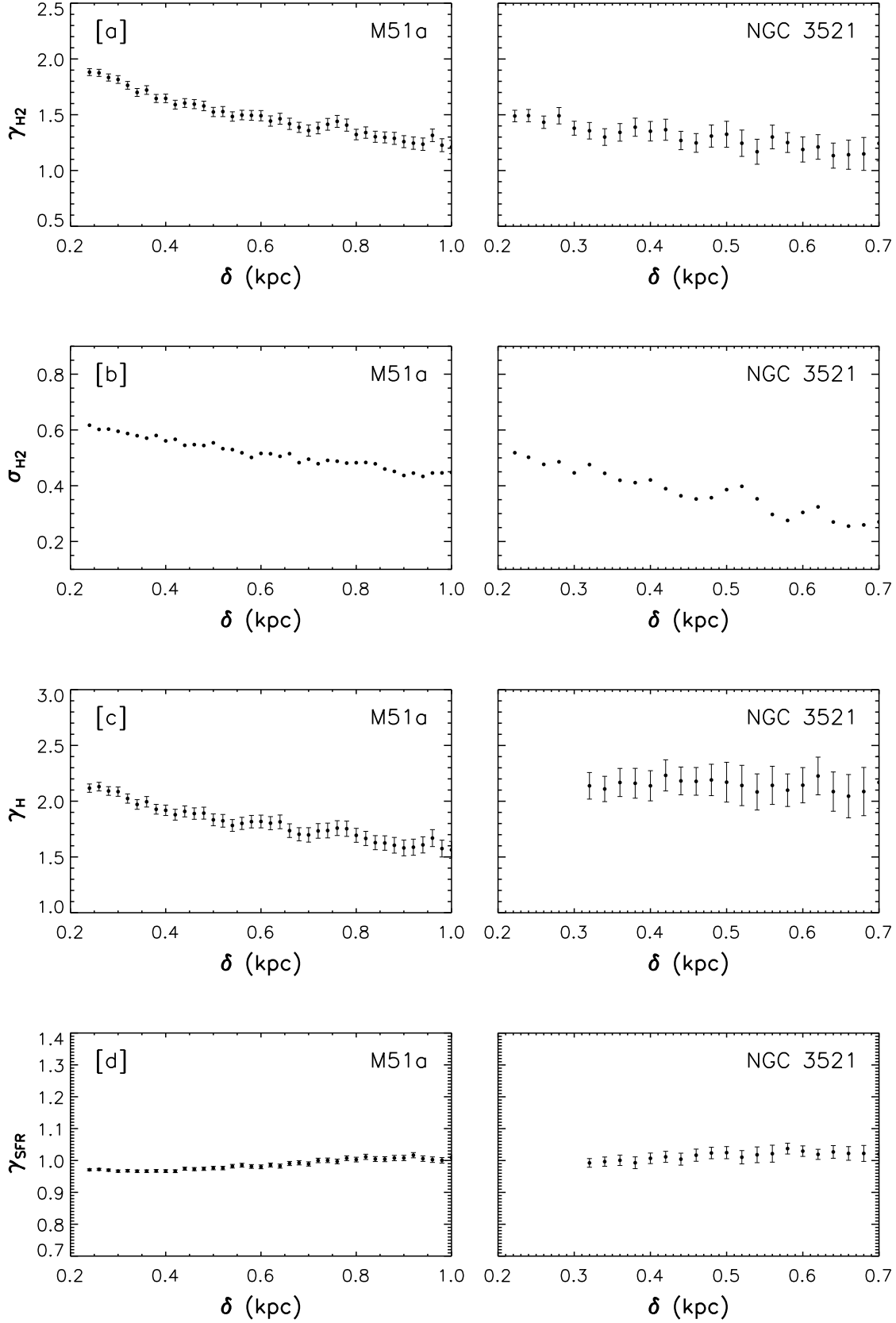
FIG. 7.— Best-fit parameters as a function of apparent resolution ($\delta$): [a] the power index of molecular-only S-K law; [b] the r.m.s. dispersion of the data about the best-fit molecular S-K law in unit of dex; [c] the power index of the total-hydrogen S-K law (requiring $3\sigma$ or better detection in both H I and CO maps); [d] the power index of FUV+24 $\mu$m SFR vs. H$\alpha$+24 $\mu$m SFR correlation. Note that from [a] to [c] the SFR is derived from H$\alpha$+24 $\mu$m luminosity.
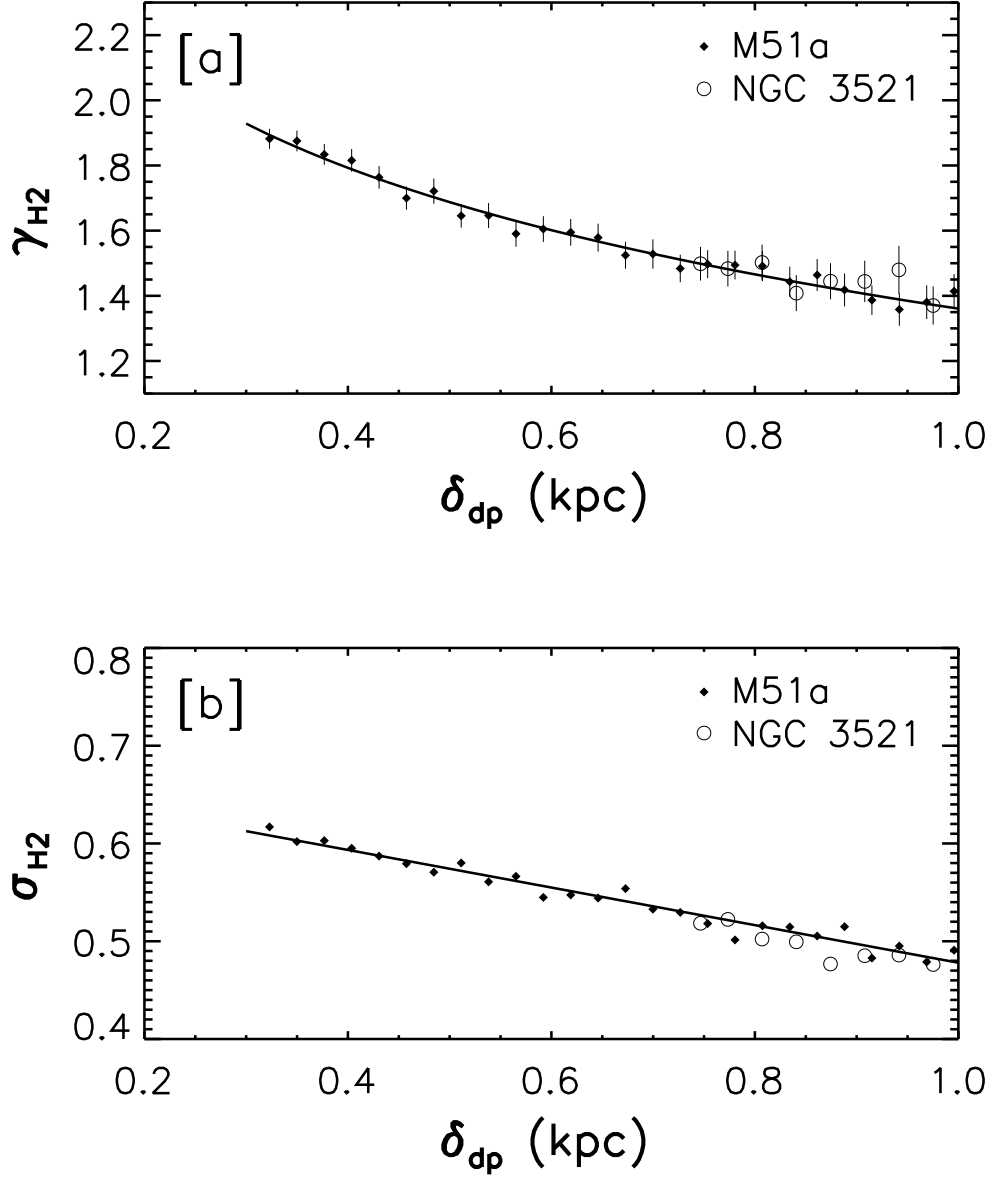
FIG. 8.— The power index ($\gamma_{H_2}$) and r.m.s. dispersion ($\sigma_{H_2}$) of the best-fit molecular S-K law in M51a and NGC 3521, plotted as a function of de-projected resolutions ($\delta_{dp}$). Both quantities match remarkably well at a given $\delta_{dp}$, suggesting a shared behavior of sub-kpc molecular S-K law in them. Fitting to the data points of M51a only, we find the logarithmic function $\gamma_{H_2} = -1.09 \log [\delta_{dp}/kpc] + 1.36$ and the linear relation $\sigma_{H_2} = -0.19 [\delta_{dp}/kpc] + 0.67$ are able to depict the behavior of these two quantities in both galaxies remarkably well, as over-plotted with solid lines in [a] and [b], respectively.
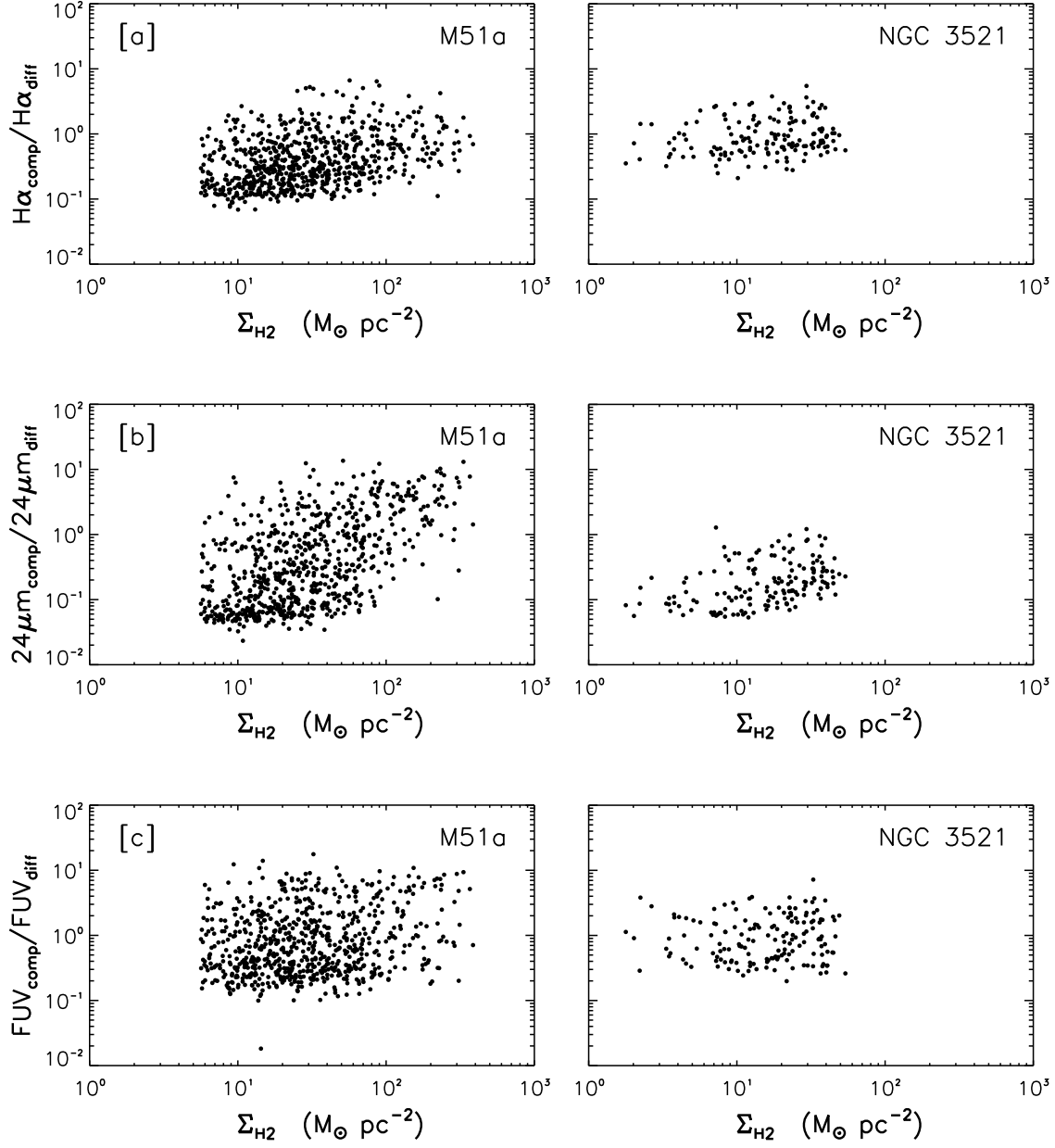
Liu et al.



FIG. 9.— The compact-to-diffuse ratio of emission in: [a] H$\alpha$, [b] 24 $\mu$m and [c] FUV, ploted as a function of $\Sigma_{H_2}$. Only $>3\sigma$ pixels are taken into account. For both M51a and NGC 3521, the projected resolution examined is 400 pc. Note the broader range of variation in 24 $\mu$m than in H$\alpha$ and FUV.

TABLE 1
Best-fit parameters of the sub-kpc molecular S-K law in M51a (3-$\sigma$ thresholds are applied), expressed as $\Sigma_{\mathrm{SFR(H\alpha+24\mu m)}} = A\,\Sigma_{\mathrm{H_2}}^{\gamma_{\mathrm{H_2}}}$ with an r.m.s. dispersion $\sigma_{\mathrm{H_2}}$ about the best-fit power scaling.

| Resolution (kpc) | $\gamma_{\mathrm{H_2}}$ | $A$ | $\sigma_{\mathrm{H_2}}$ |
|---|---|---|---|
| 0.25 | 1.86±0.03 | −5.49±0.05 | 0.60 |
| 0.30 | 1.82±0.03 | −5.36±0.06 | 0.60 |
| 0.40 | 1.65±0.04 | −4.97±0.06 | 0.56 |
| 0.50 | 1.52±0.04 | −4.71±0.07 | 0.55 |
| 0.60 | 1.49±0.05 | −4.62±0.07 | 0.52 |
| 0.70 | 1.36±0.05 | −4.36±0.08 | 0.50 |
| 0.80 | 1.32±0.05 | −4.24±0.07 | 0.48 |
| 0.90 | 1.26±0.05 | −4.14±0.08 | 0.44 |
| 1.00 | 1.21±0.06 | −4.08±0.09 | 0.45 |

TABLE 2
Best-fit parameters of the sub-kpc molecular S-K law in NGC 3521. Symbols are the same as for M51a.

| Resolution (kpc) | $\gamma_{\mathrm{H_2}}$ | $A$ | $\sigma_{\mathrm{H_2}}$ |
|---|---|---|---|
| 0.25 | 1.41±0.06 | −4.48±0.08 | 0.50 |
| 0.30 | 1.40±0.06 | −4.43±0.09 | 0.45 |
| 0.40 | 1.35±0.09 | −4.32±0.12 | 0.42 |
| 0.50 | 1.33±0.12 | −4.25±0.16 | 0.39 |
| 0.60 | 1.19±0.11 | −4.05±0.15 | 0.30 |
| 0.70 | 1.24±0.16 | −4.12±0.21 | 0.27 |

TABLE 3
Best-fit slopes of the molecular S-K law when different $\Sigma_{\mathrm{H_2}}$ thresholds are applied but the SFR (traced by H$\alpha$+24 $\mu$m) threshold is fixed at 3-$\sigma$: the case of M51a.

| Resolution (kpc) | 1-$\sigma$ | 2-$\sigma$ | 3-$\sigma$ | 4-$\sigma$ | 5-$\sigma$ |
|---|---|---|---|---|---|
| 0.25 | 1.60 | 1.77 | 1.86 | 1.97 | 2.02 |
| 0.30 | 1.51 | 1.67 | 1.82 | 1.88 | 1.97 |
| 0.40 | 1.41 | 1.54 | 1.65 | 1.72 | 1.75 |
| 0.50 | 1.33 | 1.44 | 1.52 | 1.60 | 1.66 |
| 0.60 | 1.32 | 1.43 | 1.49 | 1.56 | 1.63 |
| 0.70 | 1.20 | 1.27 | 1.36 | 1.46 | 1.48 |
| 0.80 | 1.21 | 1.28 | 1.32 | 1.38 | 1.48 |
| 0.90 | 1.10 | 1.18 | 1.26 | 1.29 | 1.32 |
| 1.00 | 1.06 | 1.15 | 1.21 | 1.30 | 1.33 |

TABLE 4
Best-fit slopes of the molecular S-K law when different $\Sigma_{\mathrm{H_2}}$ thresholds are applied but the SFR (traced by H$\alpha$+24 $\mu$m) threshold is fixed at 3-$\sigma$: the case of NGC 3521.

| Resolution (kpc) | 1-$\sigma$ | 2-$\sigma$ | 3-$\sigma$ | 4-$\sigma$ | 5-$\sigma$ |
|---|---|---|---|---|---|
| 0.25 | 1.20 | 1.31 | 1.41 | 1.47 | 1.54 |
| 0.30 | 1.19 | 1.34 | 1.40 | 1.44 | 1.49 |
| 0.40 | 1.23 | 1.26 | 1.35 | 1.35 | 1.37 |
| 0.50 | 1.22 | 1.22 | 1.33 | 1.33 | 1.33 |
| 0.60 | 1.19 | 1.19 | 1.19 | 1.26 | 1.26 |
| 0.70 | 1.24 | 1.24 | 1.24 | 1.24 | 1.35 |